AD A 131530

INVESTIGATION OF THE RAYLEIGH CRITICAL ANGLE PHENOMENON
FOR THE CHARACTERIZATION OF SURFACE PROPERTIES
PHASE II

FINAL REPORT
April 1983

Prepared For:

Air Force Office of Scientific Research
Bolling Air Force Base
Washington, D.C. 20332

**SPECTRON
DEVELOPMENT
LABORATORIES
INC.**

DTIC
SELECTE**D**
AUG 19 1983
D

DTIC FILE COPY

INVESTIGATION OF THE RAYLEIGH CRITICAL ANGLE PHENOMENON

FOR THE CHARACTERIZATION OF SURFACE PROPERTIES

PHASE II

FINAL REPORT

April 1983

SDL No. 83-2188-14F

Principal Investigator
B. P. Hildebrand

Senior Scientist
G. L. Fitzpatrick

Computer Scientist
A. J. Boland

Sponsored by:

Advanced Research Projects Agency (DOD)
ARPA Order No. 4109
Monitored by AFOSR under Contract #F49620-81-C-0040

SPECTRON
DEVELOPMENT
LABORATORIES
   INC.

Seattle Laboratory: 1010 Industry Drive
Seattle, WA 98188 (206) 575-9324

DTIC
SELECTE**D**
AUG 19 1983

D

REPORT DOCUMENTATION PAGE	READ INSTRUCTIONS BEFORE COMPLETING FORM

1. REPORT NUMBER AFOSR-TR- 83-0678	2. GOVT ACCESSION NO. AD-A131530	3. RECIPIENT'S CATALOG NUMBER
4. TITLE *(and Subtitle)* INVESTIGATION OF THE RAYLEIGH CRITICAL ANGLE PHENOMENON FOR THE CHARACTERIZATION OF SURFACE PROPERTIES, PHASE II		**5. TYPE OF REPORT & PERIOD COVERED** Final Report (November 1982–February 1983)
		6. PERFORMING ORG. REPORT NUMBER
7. AUTHOR(s) B. P. Hildebrand, G. L. Fitzpatrick and A. J. Boland		**8. CONTRACT OR GRANT NUMBER(s)** F49620-81-C-0040
9. PERFORMING ORGANIZATION NAME AND ADDRESS Spectron Development Laboratories, Inc. 1010 Industry Drive Seattle, WA 98188		**10. PROGRAM ELEMENT, PROJECT, TASK AREA & WORK UNIT NUMBERS** 61102F 2306
11. CONTROLLING OFFICE NAME AND ADDRESS Air Force Office of Scientific Research Bldg. 410 Bolling Air Force Base Washington, D.C. 20332		**12. REPORT DATE** April 1983
		13. NUMBER OF PAGES 52
14. MONITORING AGENCY NAME & ADDRESS*(if different from Controlling Office)*		**15. SECURITY CLASS. *(of this report)*** Unclassified
		15a. DECLASSIFICATION DOWNGRADING SCHEDULE

16. DISTRIBUTION STATEMENT *(of this Report)*

Approved for public release; distribution unlimited.

17. DISTRIBUTION STATEMENT *(of the abstract entered in Block 20, if different from Report)*

18. SUPPLEMENTARY NOTES

19. KEY WORDS *(Continue on reverse side if necessary and identify by block number)*

Rayleigh critical angle
Rayleigh waves
Surface waves
Pseudosurface waves
Nonlinear effects

Third order elastic constants
Higher harmonics
Anisotropy

20. ABSTRACT *(Continue on reverse side if necessary and identify by block number)*

Rayleigh type acoustic critical angle experiments on a variety of samples ranging from single crystals to polycrystalline alloys and glasses have been performed. Two conclusions can be drawn from this work: (1) simple linear equations of motion, which include anisotropy, suffice for an approximate description of the observations; (2) certain observations at and near the critical angle, involving the production of anomalous harmonics, imply that the nonlinear characteristics of the water, and possibly the solid, cannot

DD 1 FORM JAN 73 **1473**   EDITION OF 1 NOV 65 IS OBSOLETE

20. Abstract (continuted)

be ignored and need further study. Moreover, the new measuring apparatus, using an acoustic lens, has the following desirable features: (a) it allows local measurements of the solid properties to be made, and (b) except for problems associated with phase measurements of the reflected waves, experimental results are essentially consistent with the work of others who used a different experimental approach. We conclude that our goal of using a device in practical flaw imaging work is reasonable and holds promise of being a quantitative flaw imaging technique.

TABLE OF CONTENTS

LIST OF FIGURES

LIST OF FIGURES (Continued)

1.0 INTRODUCTION

In most practical applications of ultrasonics we are faced with
the problem of understanding the response of an interface (usually a
water-solid interface) to an incident longitudinal wave in water.
If deep targets lying many wavelengths within the solid are to be
investigated, the amount of energy penetrating the interface is often
of interest, whereas if the region to be investigated is near the
interface (within roughly one shear wavelength), the detailed response
of the interface must be understood.

The work reported here has focused on the latter problem and, in
particular, on the practical application of the so-called Rayleigh
critical angle phenomenon [1-13]. By properly adjusting the angle of
incidence of an incident longitudinal wave in water, it is possible
to generate a Rayleigh-type interface wave that propagates along a
water-solid interface. Such an interface wave penetrates one shear
wavelength into the solid [11] and as it propagates along the interface,
it radiates energy back into the water [14]. For this reason, such
waves are often called "leaky surface waves."

The radiated component has considerable practical significance
since it is modulated by subsurface information (information arising
in the solid within the penetration depth of the interface wave of
roughly one shear wavelength). Proper examination and interpretation
of this radiated component, which is always unavoidably mixed with a
specularly reflected component, can be expected to provide useful
information on the character of the solid material near the interface.

It is for this reason that the Rayleigh critical angle phenomenon
holds promise as a tool for materials evaluation and nondestructive
testing. Near surface defects, flaws, cracks, inclusions, etc. are
easily detected, characterized, and also imaged by observing the
influence of such anomalies on the radiated wave component.

Although such "interface problems" have been the subject of
numerous experimental and theoretical studies, the inherent complexity

of the phenomenon, when all relevant physical features are included, makes complete interpretation of experiments very difficult.

In this report we will describe a new type of experimental apparatus [12, 13] which eliminates at least one of the data interpretation problems by making possible local rather than global measurements of the interface response.

The present report begins by reviewing appropriate theory and describing some of the problems involved in interpreting interface data when the interface is treated in a realistic physical fashion. The nontrivial inverse problem, namely going from experimental data to the elastic properties of the solid, is then discussed. The effects of the focused sound source used to excite interface waves locally, including nonlinear effects, are also described.

We then turn to a description of the new apparatus and to experiments on materials ranging from those with isotropic elastic properties to those with anisotropic elastic properties.

'Images' of the phase and amplitude of the measured local reflection coefficient (corresponding to near surface defects) made by scanning the focal region of the acoustic lens over the interface are then described. The report closes with a discussion of the prospects and problems associated with further practical development.

2.0 THEORETICAL BACKGROUND

The correct (complete) classical description of the mechanical response of a water-solid interface would be a very complex affair. Such a description would correctly treat all nonlinear effects (in the water and the solid) which includes the detailed description of the transfer of linear and angular momentum at all angles of incidence and at all amplitudes however small. It would correctly treat anisotropy, nonuniformity, inhomogenity, and frictional attenuation, among other effects.

Owing to such complexities, the materials on both sides of the interface are often treated as if they were linear, isotropic, uniform and homogenous, and in many practical applications, these assumptions are valid approximations to reality.

While the simplification to a linear theory, in particular, leads to an incomplete and sometimes contradictory formalism, the practical significance of this situation for many important applications is not great. Except for the nonlinear effects seen in the water path, our experiments are well described by linear equations of motion provided anisotropy is also included where appropriate.

2.1 Anisotropy

All crystalline solids and many alloys are anisotropic [16, 23-26]. This leads to equations of motion involving the tensor properties of a material. If these anisotropic materials are assumed to be described approximately by linear equations of motion (all anharmonic effects dropped), the complete classical strain tensor, which includes nonlinearities, namely

$$U_{ik} = \frac{1}{2}\left(\frac{\partial U_i}{\partial X_k} + \frac{\partial U_k}{\partial X_i} + \frac{\partial U_r}{\partial X_i}\frac{\partial U_r}{\partial X_k}\right) \tag{1}$$

can be approximated by dropping the higher order terms to yield the linear strain tensor [16]

$$U_{ik} \simeq \frac{1}{2}\left(\frac{\partial U_i}{\partial X_k} + \frac{\partial U_k}{\partial X_i}\right) . \tag{2}$$

The classical equation of motion, which is Newton's second law, is then

$$\rho \ddot{U}_i = \partial \sigma_{ik}/\partial X_k \tag{3}$$

where ρ is the mass density and σ_{ik} is the general stress tensor

$$\sigma_{ik} = \lambda_{ik\ell m} U_{\ell m} \tag{4}$$

where $\lambda_{ik\ell m}$ gives the adiabatic modulii of elasticity and where $U_{\ell m}$ is the linear strain tensor (Eq. (2)). The equation of motion is then approximated by

$$\rho \ddot{U}_i \simeq \lambda_{ik\ell m} \frac{\partial^2 U_m}{\partial X_k \partial X_\ell} . \tag{5}$$

This approximate equation possesses only harmonic solutions. That is, no shock waves, solitons, or other nonlinear phenomena are possible owing to linearity. These harmonic solutions are

$$U_i = U_{oi} e^{i(\bar{k}\cdot\bar{r} - \omega t)} \tag{6}$$

where the wavevector $\bar{k}$ is a function of frequency ω and satisfies Eq. (5). Then substituting Eq. (6) into Eq. (5), we have

$$(\rho\omega^2 \delta_{im} - \lambda_{ik\ell m} k_k k_\ell) U_m = 0 \tag{7}$$

and the effects of anisotropy are evidently contained in the elasticity tensor $\lambda_{ik\ell m}$.

This equation represents three homogeneous equations in the unknown particle displacement $U_1 = U_x$, $U_2 = U_y$, and $U_3 = U_z$. Nontrivial solution requires that the determinant of the coefficients vanish

$$|\lambda_{ik\ell m} k_k k_\ell - \rho\omega^2 \delta_{im}| = 0 . \tag{8}$$

This last equation is seen to be a cubic in ω^2 since i, k, ℓ, m = 1, 2, 3. Each of the three roots of this equation provide a functional relation between frequency ω and wavenumber k. Hence, there are, in general, three kinds of independent motion and three characteristic velocities in an unbounded anisotropic linear solid. Two roots of Eq. (8) correspond to bulk quasi-transverse waves and one to a bulk quasi-longitudinal wave.

The existence of multiple bulk waves in an anisotropic solid greatly complicates the interface problem. In particular, it is found that two Rayleigh type interface waves are generally produced, whereas only one Rayleigh type wave is produced at a water isotropic solid interface [27-32]. Moreover, energy flux directions generally deviate from wavevector directions in anisotropic solids, making simple data analysis based on Snell's law (as applied to water isotropic solid interface) generally invalid.

2.2 Interface Waves in Linear Isotropic Materials

The foregoing description of a linear anisotropic material is in basic agreement with experience for many applications. This general formulation includes the special case of a linear isotropic solid where the equation of motion in vector notation is approximated by [16]

$$\rho\ddot{\overline{U}} \simeq \mu\nabla^2\overline{U} + (\lambda + \mu)\nabla(\nabla\cdot\overline{U}) \tag{9}$$

-5-

and where λ and μ are the two Lamé coefficients which can also be written in terms of the Young's modulus E and Poisson's ratio σ as

$$\lambda + \mu = \frac{E}{2(1 + \sigma)(1 - 2\sigma)} \tag{10}$$

$$\mu = \frac{E}{2(1 + \sigma)} \quad . \tag{11}$$

In terms of the second order elastic constants C_{ij}, we also have

$$C_{11} = C_{22} = C_{33} = (\lambda + 2\mu) \tag{12}$$

$$C_{12} = C_{21} = C_{13} = C_{31} = C_{23} = C_{32} = \lambda \tag{13}$$

$$C_{44} = C_{55} = C_{66} = \mu \quad . \tag{14}$$

In such a linear isotropic material, it is possible to think of the particle displacement $\overline{U}$ as being decomposed into just two kinds of independent motions because of linearity, namely

$$\overline{U} = \nabla\phi + \nabla\times\overline{\Psi} \tag{15}$$

where ϕ and $\overline{\Psi}$ are, respectively, the scalar and vector "potentials" describing the displacement $\overline{U}$. Thus, $\overline{U}$ consists of a dilational part $\nabla\phi$ (characterized by a volume change) and a rotational part $\nabla\times\overline{\Psi}$ (volume invariant). Substitution of $\overline{U}$ into Eq. (9) gives two equations of motion, one for ϕ and one for $\overline{\Psi}$, namely

$$\nabla^2\phi - \frac{1}{C_L{}^2} \frac{\partial^2\phi}{\partial t^2} = 0 \tag{16}$$

where C_L is the bulk longitudinal wave velocity

$$C_L{}^2 = \frac{(\lambda + 2\mu)}{\rho} = \frac{E(1 - \sigma)}{\rho(1 + \sigma)(1 - 2\sigma)} \tag{17}$$

and $\quad \nabla^2\overline{\Psi} - \frac{1}{C_T{}^2} \frac{\partial^2\overline{\psi}}{\partial t^2} = 0 \tag{18}$

where C_T is the bulk transverse wave velocity

$$C_T^2 = \mu/\rho = \frac{E}{2\rho(1 + \sigma)} \ . \tag{19}$$

2.3 "Rayleigh" Critical Angle Measurements

In addition to two bulk wave solutions in an isotropic solid, there are surface wave solutions on a free surface (no water loading) which propagate at the velocity C_R given by

$$C_R = C_T \eta \tag{20}$$

where η is the single root of the Rayleigh characteristic equation [11]

$$\eta^6 - 8\eta^4 + 8\eta^2 \left(3 - 2\frac{C_T^2}{C_L^2}\right) - 16\left(1 - \frac{C_T^2}{C_L^2}\right) = 0 \tag{21}$$

having the value $|\eta| < 1$. This is given approximately by [11]

$$\eta_R = \frac{.87 + 1.12\sigma}{1 + \sigma} \ . \tag{22}$$

Here, C_T and C_L are, respectively, the transverse and longitudinal velocities and σ is Poisson's ratio. These waves are the so-called Rayleigh waves that propagate on a vacuum-solid interface. They are characterized by a rapid reduction in amplitude as a function of distance from the boundary and penetrate roughly one wavelength below the solid surface.

Even with liquid loading, the surface waves propagate along the liquid-solid interface with essentially the same velocity C_R. However, when liquid loading is present, a new and very useful feature enters as illustrated in Fig. 1. The propagating surface waves "leak" back into the water, combine, and interfere with the specularly reflected wave.

-7-

Incident Wave

Reflected and Radiated Components

z

θ   θ

2.5 cm

10 cm

Beam Profile

Liquid

"Leaky" Surface Wave

Solid

Focus

x
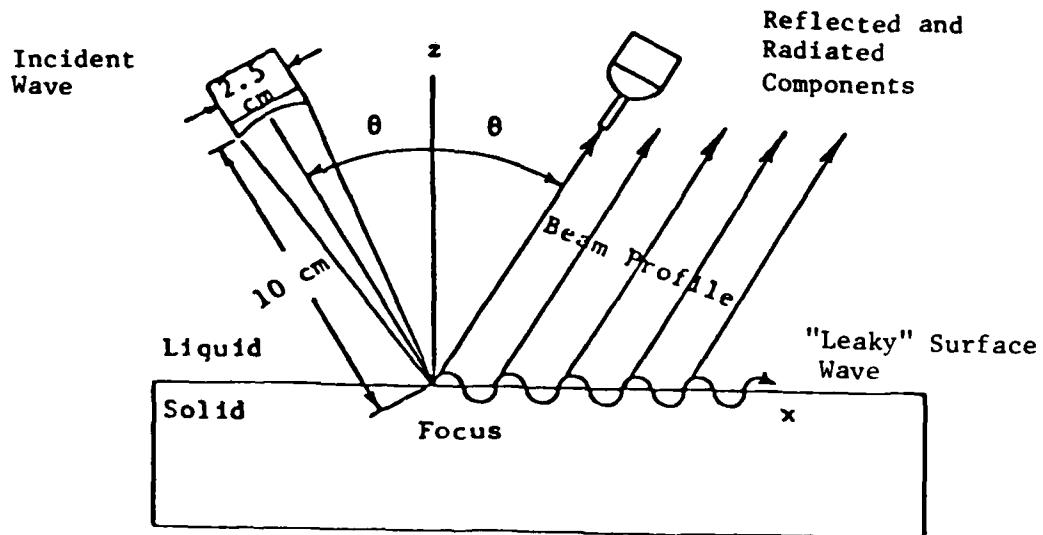
Figure 1. Focused acoustic source and point receiver combination used in experiments. The source has an aperture of 2.54 cm and a 10 cm focal length. The transducer had a 5 MHz center frequency and is typically driven at 10 volts peak-to-peak (at various frequencies 1-10 MHz). Amplitudes recorded by the point detector are typically in the 1 volt range away from the critical angle while they are typically in the millivolt range at the critical angle.

Various investigators have studied the resultant nonspecular reflection field obtaining expressions for the reflection coefficient under various conditions [28], [5]. In general, the reflection coefficient for a spatially unbounded beam may be written following Richardson [5] as (linear isotropic solid)

$$R = \frac{\cos^2 2\gamma_{22} + (c_{22}/c_{12})^2 \sin 2\gamma_{12} \sin 2\gamma_{22} + \rho_1 c_{11} \sin\gamma_{12}/\rho_2 c_{12} \sin\gamma_{11}}{\cos^2 2\gamma_{22} + (c_{22}/c_{12})^2 \sin 2\gamma_{12} \sin 2\gamma_{22} - \rho_1 c_{11} \sin\gamma_{12}/\rho_2 c_{12} \sin\gamma_{11}} ,$$

(23)

where c_{12} = velocity of longitudinal waves in the solid,

c_{22} = velocity of shear waves in the solid,

c_{11} = velocity of longitudinal waves in the liquid,

$\theta = \gamma_{11}$ = angle of incidence of the longitudinal wave in the liquid,

γ_{12} = angle of refracted longitudinal wave in the solid,

γ_{22} = angle of refracted shear wave in the solid

ρ_1 = density of liquid,

ρ_2 = density of solid.

Angles are measured in the counterclockwise direction from the plane of the interface. The velocities are the complex quantities

$$c = v(1 + iv\alpha/\omega), \tag{24}$$

v = normal velocity,

α = attenuation,

ω = radian frequency.

The refracted angles are found by the generalized Snell's law,

$$\frac{\cos\gamma_{ij}}{c_{ij}} = h . \tag{25}$$

The reflection coefficient exhibits a sharp dip and a phase shift at the so-called Rayleigh critical angle θ_R where ($C_{11} = V_w$ = longitudinal wave velocity in water)

$$\sin\theta_R \simeq \frac{V_w}{C_R} . \tag{26}$$

The above discussion applies to isotropic materials such as, crystals with small anisotropy parameters or glasses and polycrystalline alloys with no appreciable residual stresses or grain alignments. When anisotropies are present, the problem is much more complex since Eq. (26) breaks down and the phenomenon of multiple surface wave critical angles occurs.

3.0 QUALITATIVE ANALYSIS OF THE EFFECT OF CONVERGING BEAMS

Figures 1 and 2 illustrate the basic experimental arrangement and the associated electronic apparatus including an IBM personal computer which controls the system. The heart of the system is the goniometer which is provided with a computer controlled stepper motor for changing the angle of incidence (θ) of the acoustic lens axis. Data analysis and display functions are also carried out by the computer. Data is stored on disk, displayed on a CRT and/or printed out on paper. The system possesses a number of interesting capabilities including the ability to produce scanned images of the interface properties. We may also perform spectral analyses of the reflected and radiated signals. The convergent beam of sound is different than other measurement methods, however, and the question can certainly be raised as to whether our measurements are comparable to those made by different means. In this section we provide an initial analysis of our experiment based upon well known optics and acoustics theory.
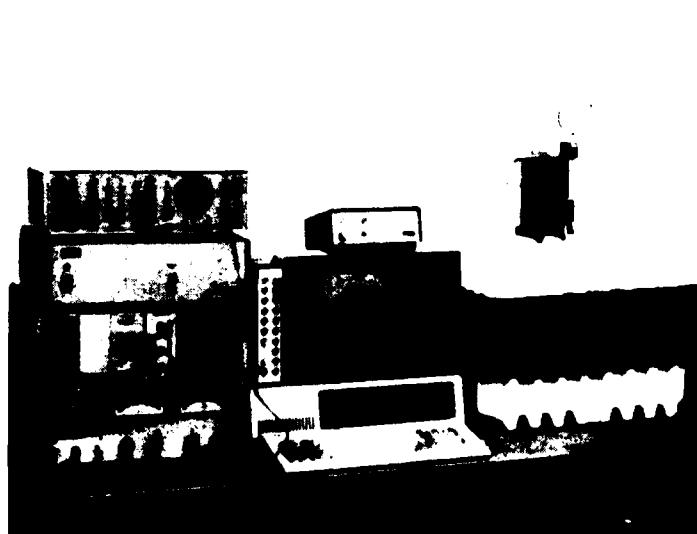
Fig. 2. Experimental Apparatus; IBM computer and display (center), goniometer and water bath (right), and electronics (left). Temperature for all measurements was maintained at 20°C by means of the water bath and the insulated tank at the right in this figure.

3.1 Plane of Incidence

In order to obtain high resolution critical angle images as described in our initial proposal, we chose the geometry shown in Fig. 3. The transmitter crystal is followed by a lens which focuses the sound to a point at the center of rotation of the goniometer. The sample is placed with its surface also at the center of rotation, and its surface normal in the plane of the goniometer. The receiving transducer consists of a very small element placed on the other arm of the goniometer. The central ray of the transmitter, and the receiver fulfill the specular reflecting geometry.

The experiment is performed by energizing the transmitter with a continuous sine wave at the appropriate frequency and monitoring the receiver with a vector volt meter. The sample is placed in the x-y plane and the goniometer carrying the transducers is moved from a small angle to a large one or vice versa. In this process, the transducers pass through all three critical angles, θ_L, θ_T, θ_R (longitudinal, transverse, and Rayleigh, respectively). The complex reflectivity as a function of angle is the recorded variable.

In the past, this type of experiment has been performed with large transducers and plane waves. Therefore, each of the critical angles mentioned above was interrogated separately, except perhaps for θ_T and θ_R which lie quite close together for some materials. In our geometry, the focused cone can sometimes contain all three critical angles. Therefore, in addition to the Rayleigh surface wave, there may be lateral waves which then radiate to form head waves that will be seen by the receiver. For our usual geometry, a 25 mm transmitter is focused at 100 mm resulting in a converging cone of 14.25° included angle. In aluminum, for example, θ_L = 13° 26', θ_T = 29° 20' and θ_R = 31° 36'. Hence, θ_L and θ_T could not be encompassed simultaneously although a slightly larger transducer could do this. θ_T and θ_R are, however, often energized together. Thus, a Rayleigh and
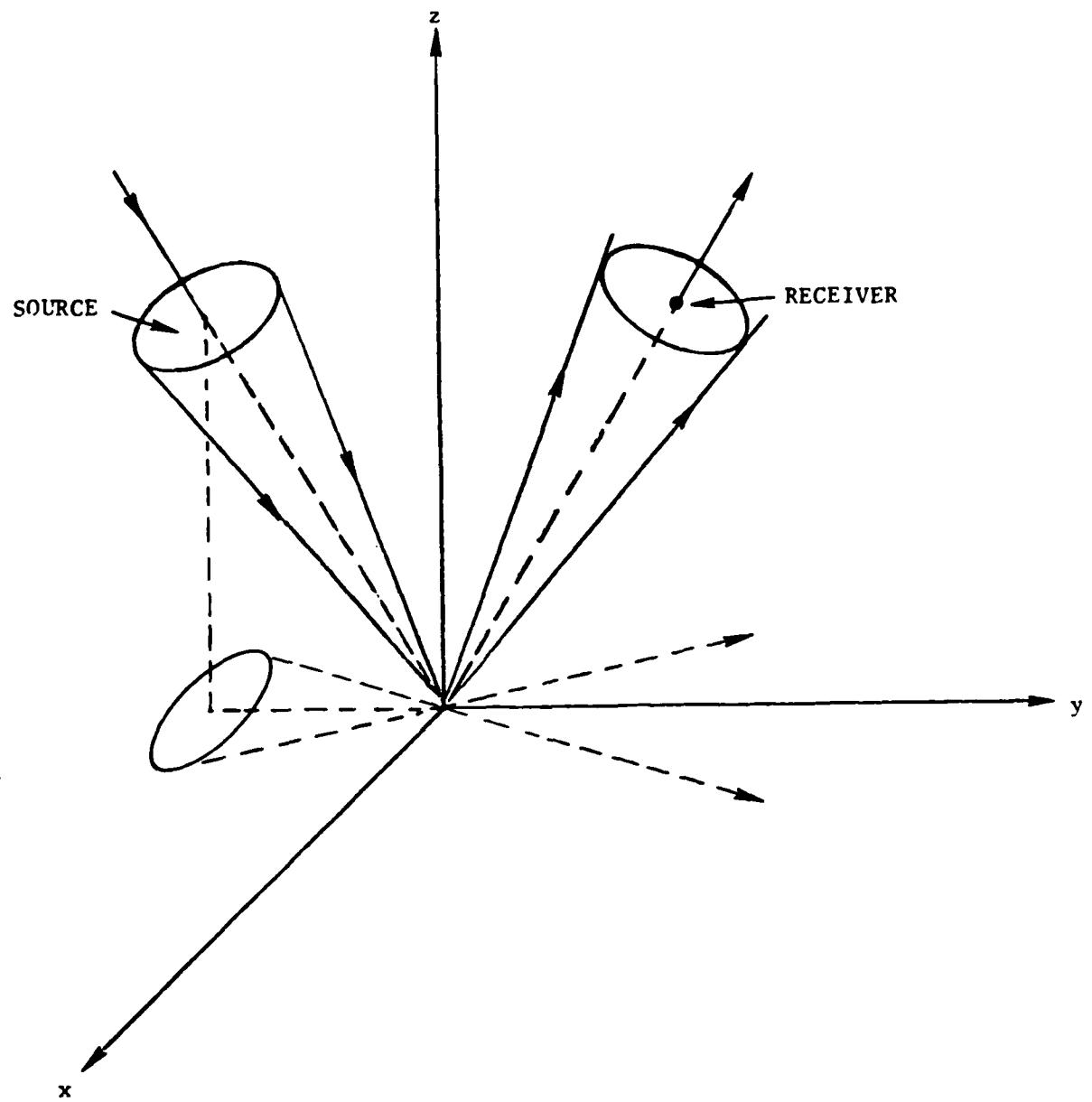
Fig. 3. Isometric sketch of the experimental system.

lateral wave will often be present simultaneously. Both of these
waves will generate head waves in the water which will be seen by
the receiver.

3.2 Plane of Solid

Returning to Fig. 3, we see that surface waves are generated
over a wedge of angles emanating from the focal point on the surface.
This wedge of surface waves reradiates a head wave back into the water,
and therefore, must make a contribution to the detected signal.

The wedge of surface waves predicted by geometric theory, as
shown in Fig. 4, will subtend an angle Ψ' which depends on the angle of
incidence of the lens axis θ, and the angle subtended by the lens
aperture from the lens focus Ψ.

$$\Psi' \simeq 2\tan^{-1}\left[\frac{\tan(\Psi/2)}{\sin\theta}\right] \tag{27}$$

Thus, the wedge of surface waves always has an opening angle Ψ'
which is somewhat larger than the opening angle of the lens Ψ.

From the foregoing, it is clear that we cannot avoid contributions
at the detector from waves radiated by the wedge of surface waves.
However, it is not evident that this will lead to results differing
significantly from those expected for incident plane waves.

From a geometrical standpoint, we note that a wedge of surface
waves will produce a conically shaped diverging wave front, as shown
in Fig. 4, of radiated waves which impinge on the point detector.
These conical surfaces will be characterized by a cone with opening angle
Ψ and an axis parallel to the axis of the lens in the plane of incidence.

The specularly reflected incident rays will produce a diverging
spherical wave front which also impinges on the same detector. The
phase difference between the conical (nonspecular reflected) and spher-
ical (specularly reflected) wave fronts in the plane of incidence should

-13-
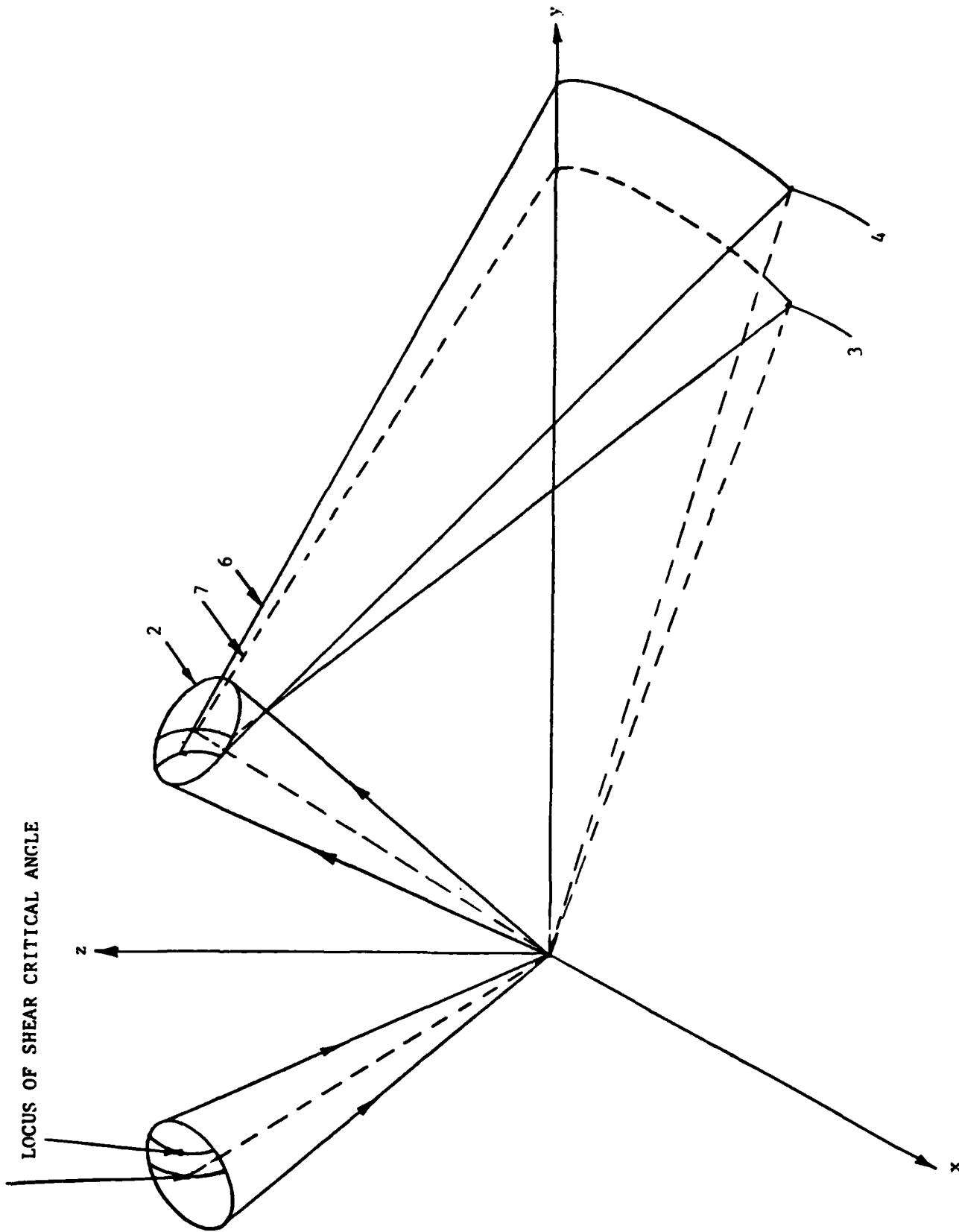
Fig. 4. Isometric sketch of the wave fronts generated by a spherical source focused at the surface of a solid.

LOCUS OF RAYLEIGH CRITICAL ANGLE

LOCUS OF SHEAR CRITICAL ANGLE

-14-

be the same as the phase difference between an incident specularly reflected plane wave and its nonspecularly reflected counterpart which is also plane. Away from the plane of incidence, of course, this statement no longer holds. Thus, if a very small point detector is used, the effect of off-axis rays should be greatly reduced if not eliminated entirely.

For example, in experiments on quartz and copper, we obtain results that are very similar to those of other investigators who assumed incident plane wave fronts. Thus, we conclude that even for aniso-tropic materials (which will distort the radiated conical wave fronts) off-axis excitation will probably not have a major effect on measurements involving a point detector.

4.0 EXPERIMENTAL RESULTS

The results of measurements performed on a 4340 steel specimen
are illustrated in Fig. 5. See Fig. 6 for a description of the angles
involved. From Fig. 5 it might at first appear that the entire specimen
is isotropic. That is, since the critical angle is close to $\theta \simeq 31.5°$
for all orientations ϕ, there would appear to be only two elastic
constants (λ and μ or E and σ), and the equation of motion would be

$$\rho \ddot{\overline{U}} \simeq \mu \nabla^2 \overline{U} + (\lambda + \mu)\nabla(\nabla \cdot \overline{U}) \qquad (28)$$

admitting only Rayleigh type surface wave solution [11]. Thus,
only one Rayleigh type critical angle would be expected. Note,
however, that these measurements characterize a region on the liquid-
solid interface which measures roughly only one wavelength in water
($\lambda \simeq .04$ cm) in diameter.

We have found other regions on this same specimen (not illustrated)
that are anisotropic and exhibit more than one critical angle. This
observation demonstrates how the focused lens source and point receiver
combination allow us to "map" or "image" the local elastic properties
at different points on a surface, in principle. A true isotropic
material namely, optical glass, also shows a single critical angle at
$\theta_{cr} \simeq 28.5°$ as illustrated in Fig. 7. Unlike the 4340 steel specimen,
however, there are no regions of appreciable anisotropy in the glass
specimen so that one critical angle characterizes the entire specimen.

Figures 8 and 9 illustrate data taken on a single crystal
of copper. This illustrates the ability of the measurement system
to orient such a crystal. Since copper is cubic (see Fig. 10),
rotation about the (100) axis would be expected to produce critical
angles showing the 90° periodicity (with ϕ) observed in Fig. 8.
Thus, the axis of rotation was in fact the (100) axis and the
copper crystal has been oriented using critical angle measurements.
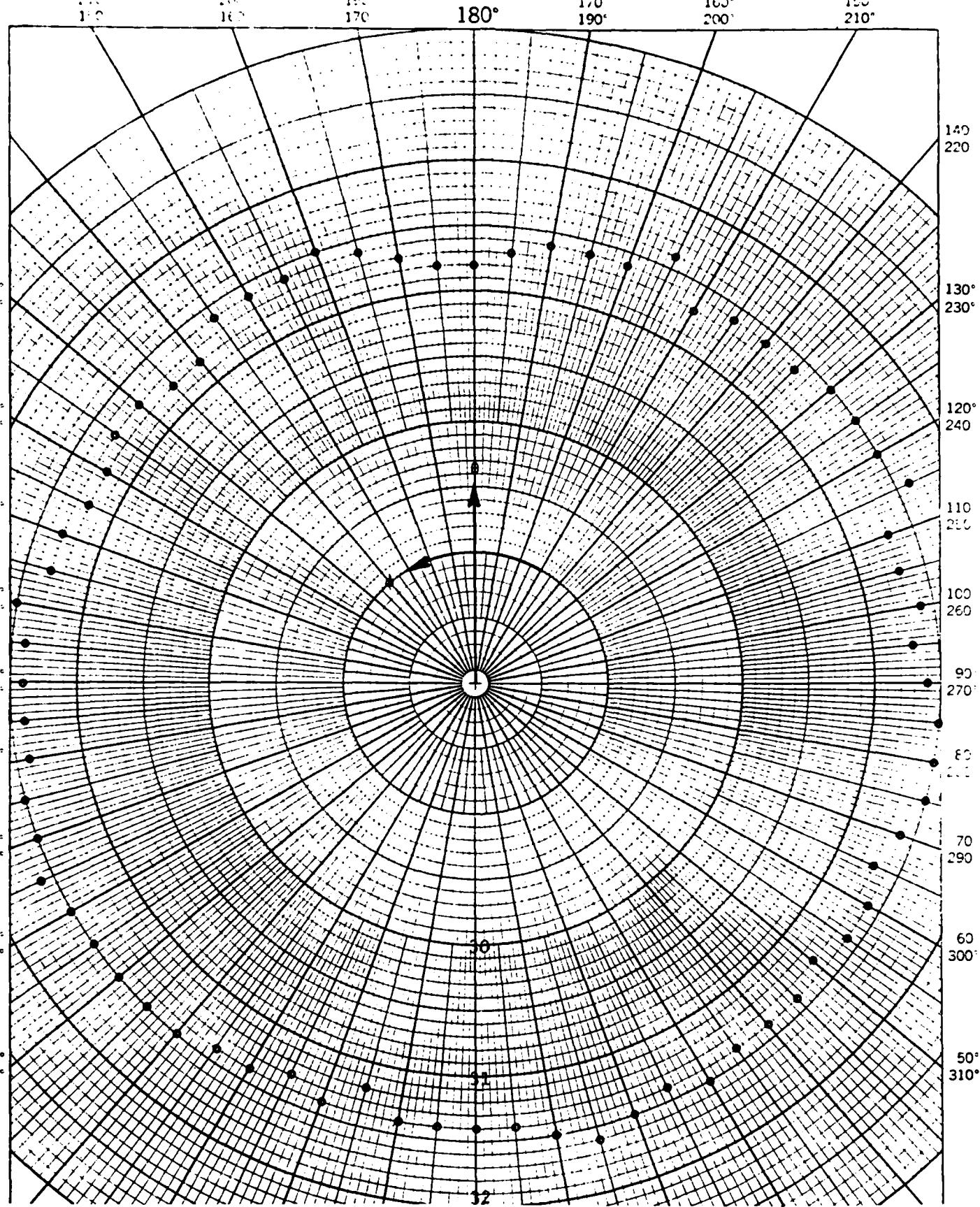
Fig. 5. Critical angles (θ) vs φ for a 4340 steel sample. The frequency was 4.1 MHz, temperature 20°C, and source oscillator amplitude 6.5 volts. The material appears to be approximately isotropic in the small region of measurement (the lens focus).

-17-
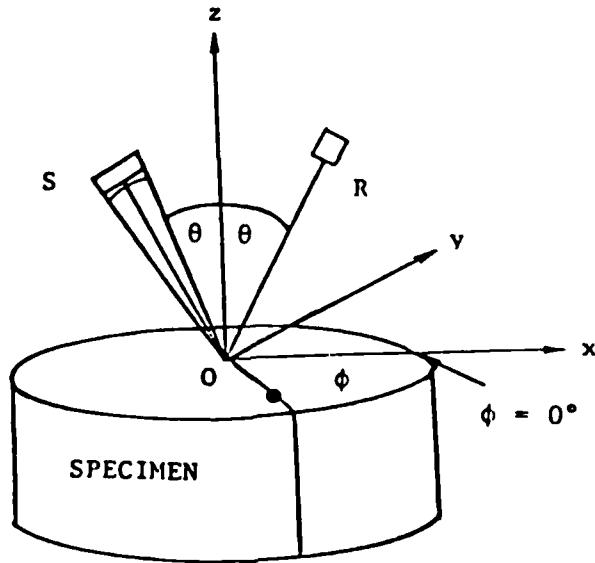
Fig. 6. Rotation of Samples. Samples are arbitrarily marked with
a spot as shown. The spot is located along the positive
x-axis which initially lies in the incident plane (S-O-R)
of the source and receiver. The normal to the specimen
surface lies along the z-axis for all azimuthal angles ϕ.
We arbitrarily label the x direction $\phi = 0°$ and turn the
specimen counterclockwise.
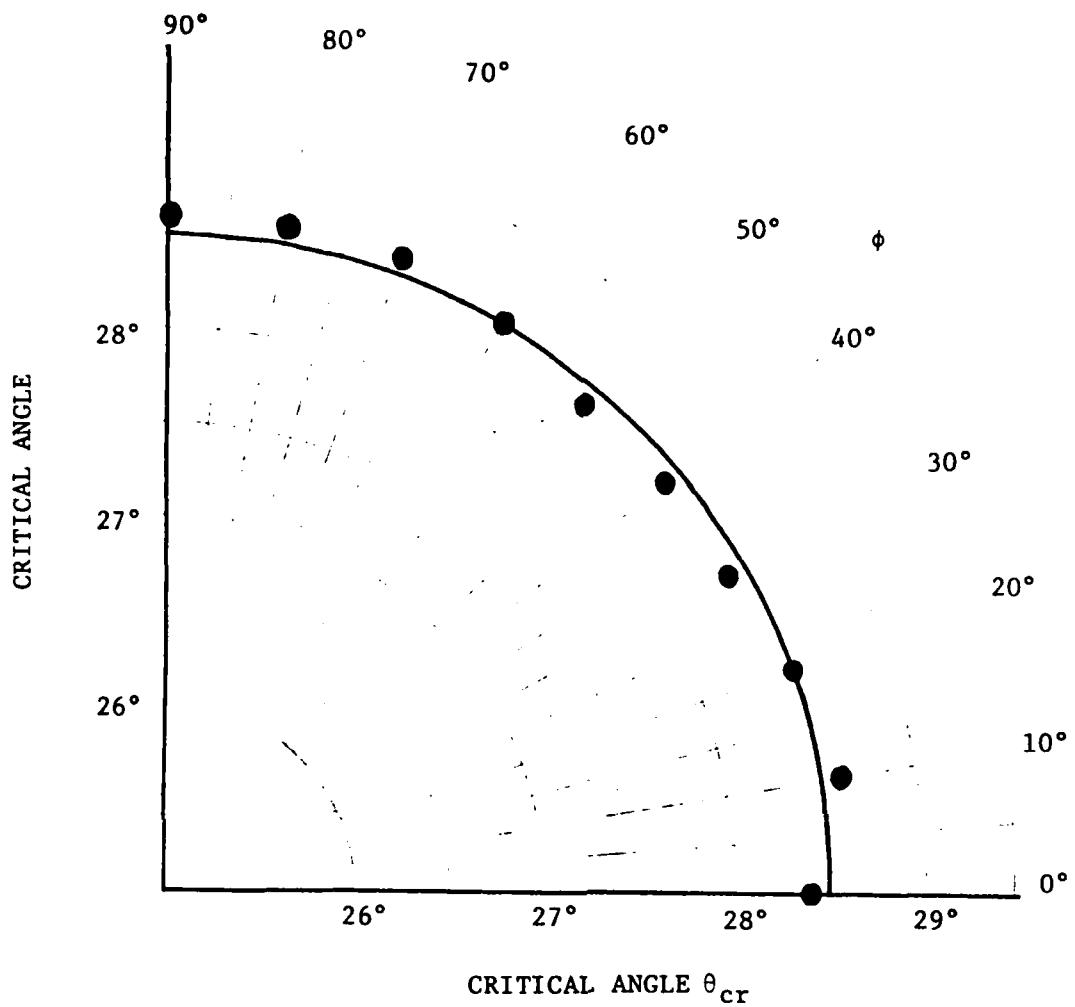
Fig. 7. Critical angle for glass. The figure shows the critical angle as a function of the azimuthal angle ϕ (angle of rotation of the specimen).
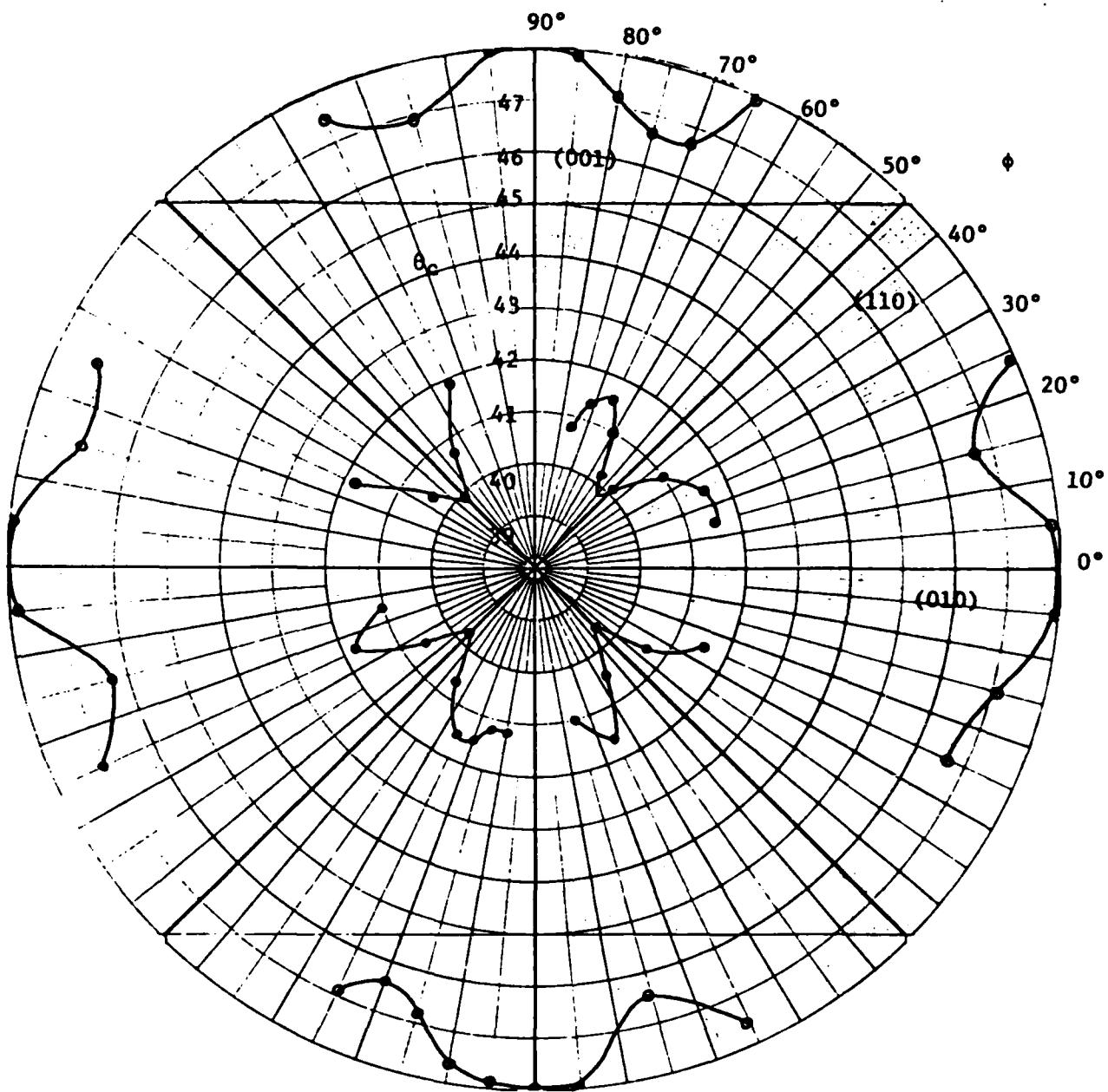
Fig. 8. Rayleigh-type (surface wave) critical angles for a
copper single crystal rotated about the (100) axis.
The frequency was 3.8 MHz and the two critical angles
occur at $\theta_c \simeq 41°$ and $\theta_c \simeq 47°$. The azimuthal angle
ϕ (angle of rotation about the 100 axis) varied from
0 to 360° and data was taken in steps of $\Delta\phi = 5°$.
Pure mode directions (001, 110, and 010) are marked
on the figure.
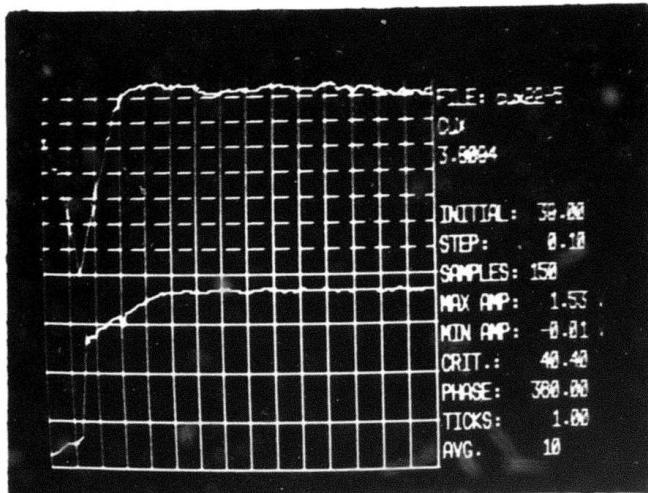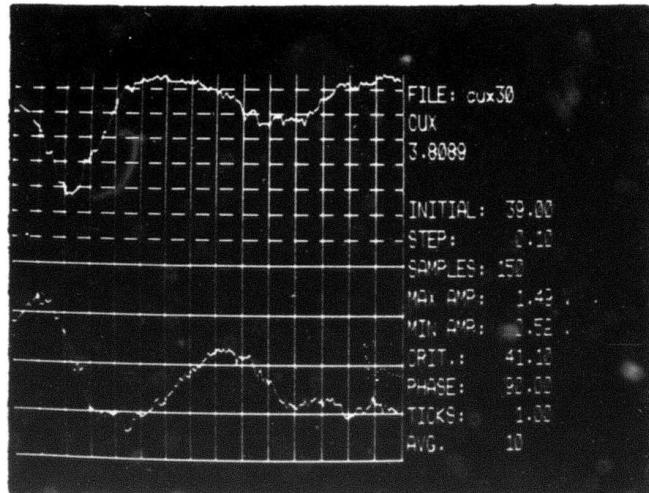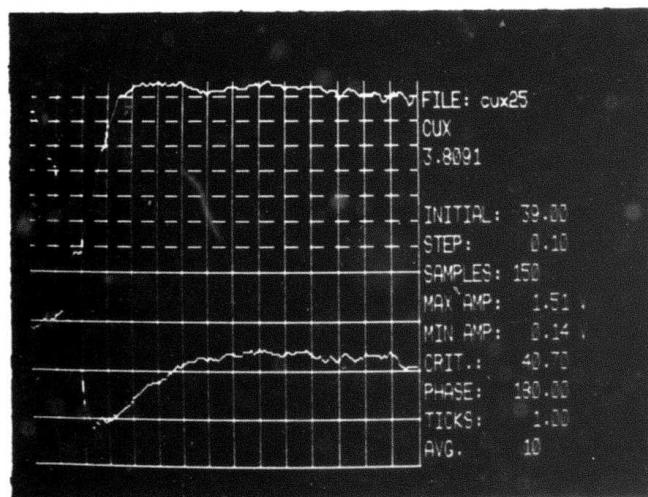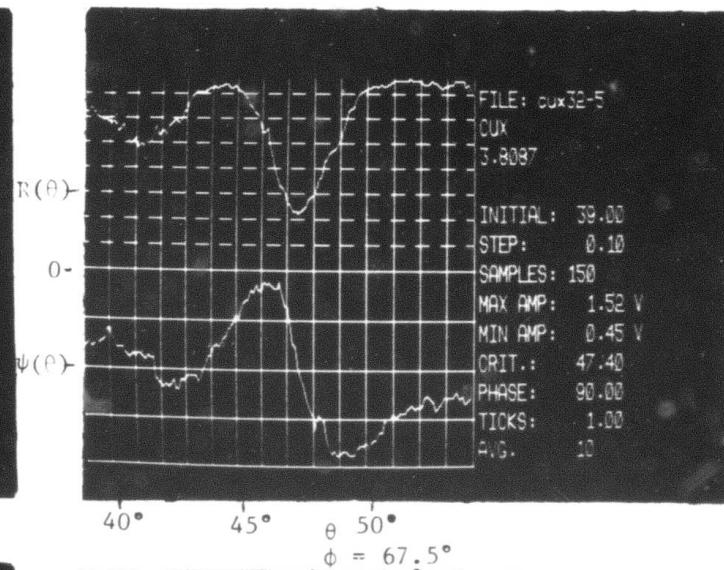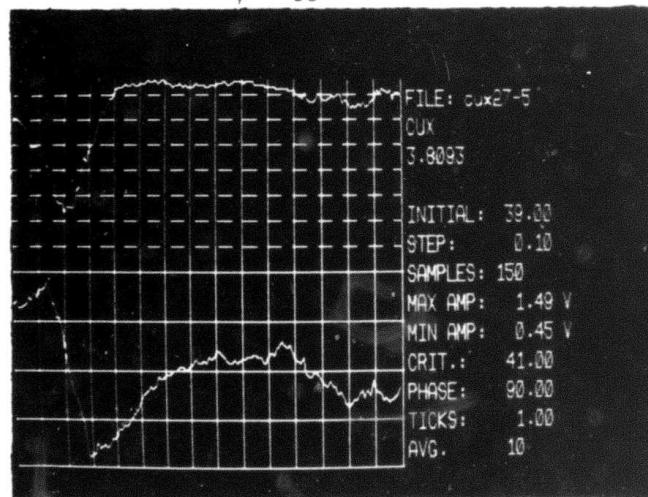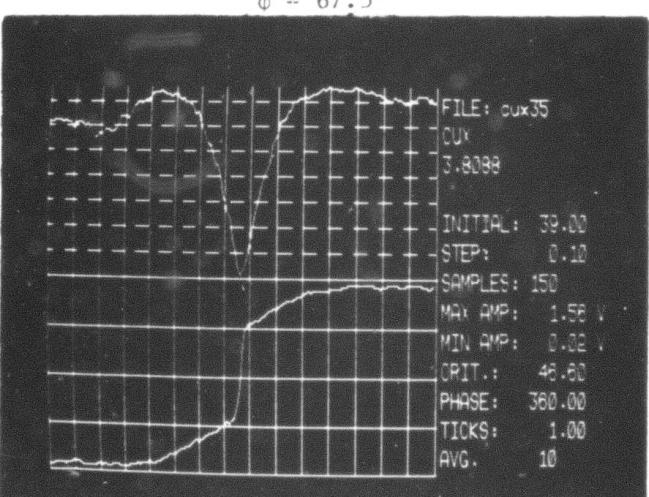
Fig. 9. Amplitude $R(\theta)$ and phase $\psi(\theta)$ vs θ for different azimuthal angles ϕ for the copper single crystal (angle of rotation ϕ about the 100 axis).

(a) (111) axis
(111) plane edge on   (b) (100) axis   (c) (110) axis
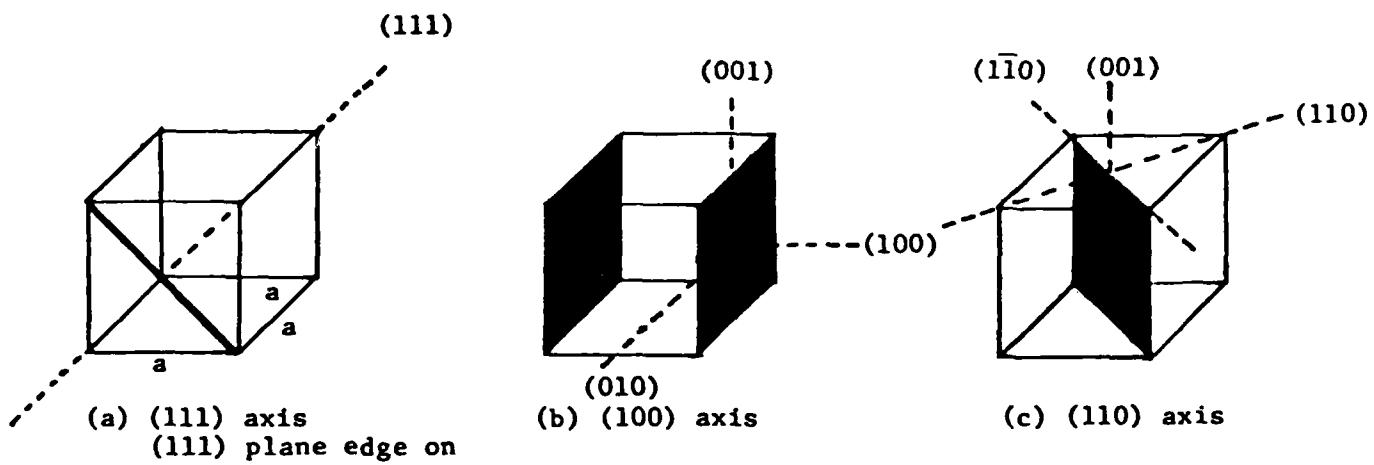
Fig. 10. Miller indices for cubic crystals. The axes are perpen-
dicular to the shaded planes of the same designation.
That is, the 100 axis is perpendicular to the 100 plane.
Many directions are quivalent in a cubic crystal. For
example, the 100 direction is equivalent to the 001
direction or the 010 direction in so far as bulk elastic
properties are concerned.

Not all crystals may be oriented, however, as illustrated by the measurements made on an aluminum single crystal. The crystal of aluminum, having a very low anisotropy parameter [24-26], looks very nearly isotropic as illustrated by the critical angle measurements of Fig. 11. Clearly, such crystals cannot be oriented easily using critical angle measurements alone.

Finally, in Fig. 12 we illustrate a series of measurements made on a titanium alloy with varying O_2 content. One population of samples (two samples) with different but "low" O_2 content (A and B) seem to have more or less isotropic characteristics. But, above a certain O_2 content (samples C, D, and E) all of the samples appear to be anisotropic owing to the distinct elliptical patterns exhibited by curves of θ versus ϕ as in Fig. 12. Although the data is sketchy (more points on a given sample should be examined and averaged, for example), it does appear that a change in crystal structure has taken place above a threshold O_2 content. In particular, below this threshold the anisotropy parameter is small and above this threshold it is large. Although the detailed reasons for such behavior reside in the domain of metallurgy (wavelength exceeds sizes of crystallites so that a long range correlation or alignment over many crystallites, which depends on O_2 content, appears to take place at specimen C), it is clear that acoustic critical angle techniques might be helpful in characterizing or signaling the onset of such changes of the crystalline symmetry character of a specimen.
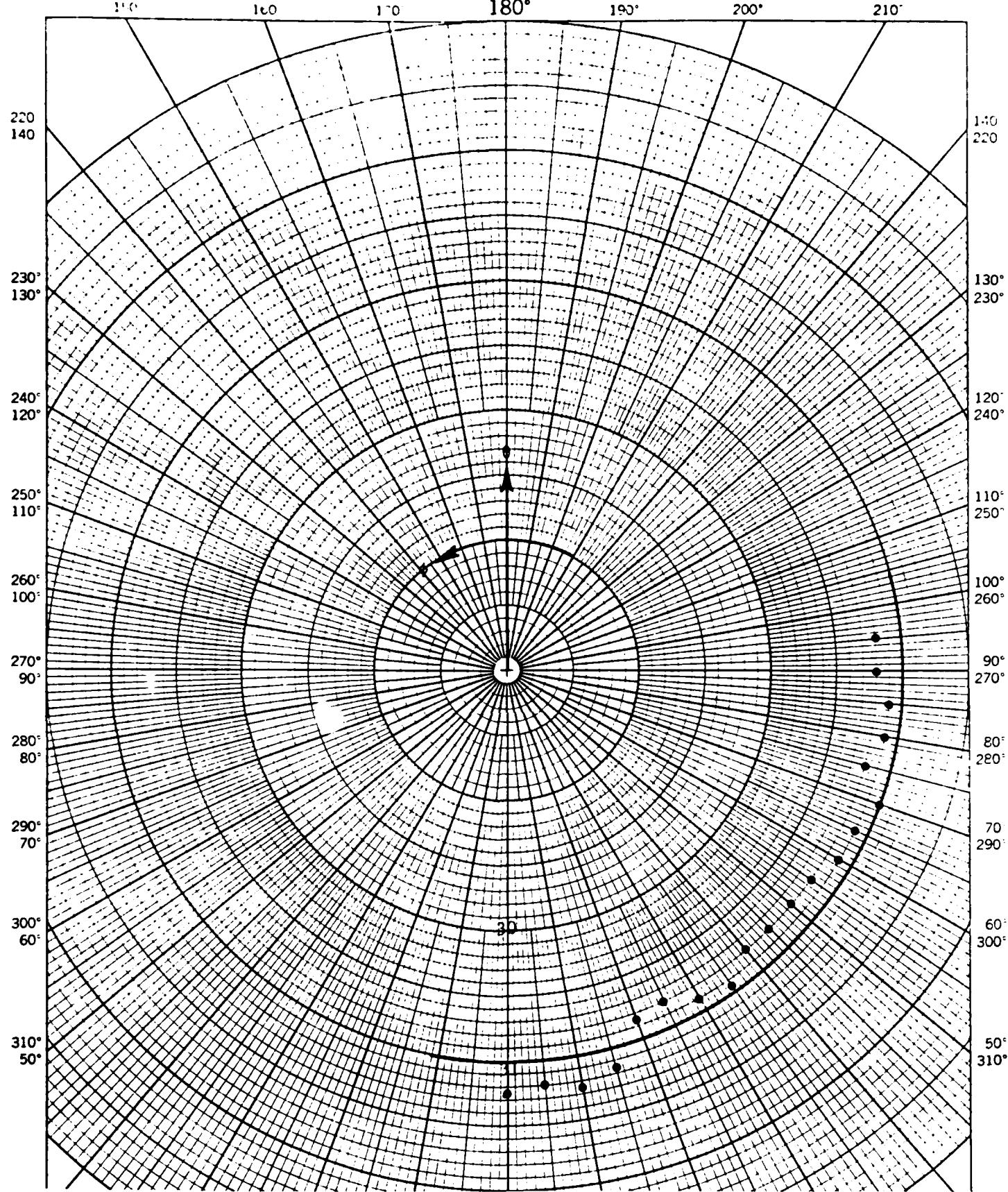
Fig. 11. Critical angles (θ) vs φ for an aluminum single crystal. The
frequency was 3.8 MHz, temperature 20°C, and source oscillator
amplitude 9 volts. The axis of rotation was coincident with
the (100) axis of this cubic crystal.

-24-
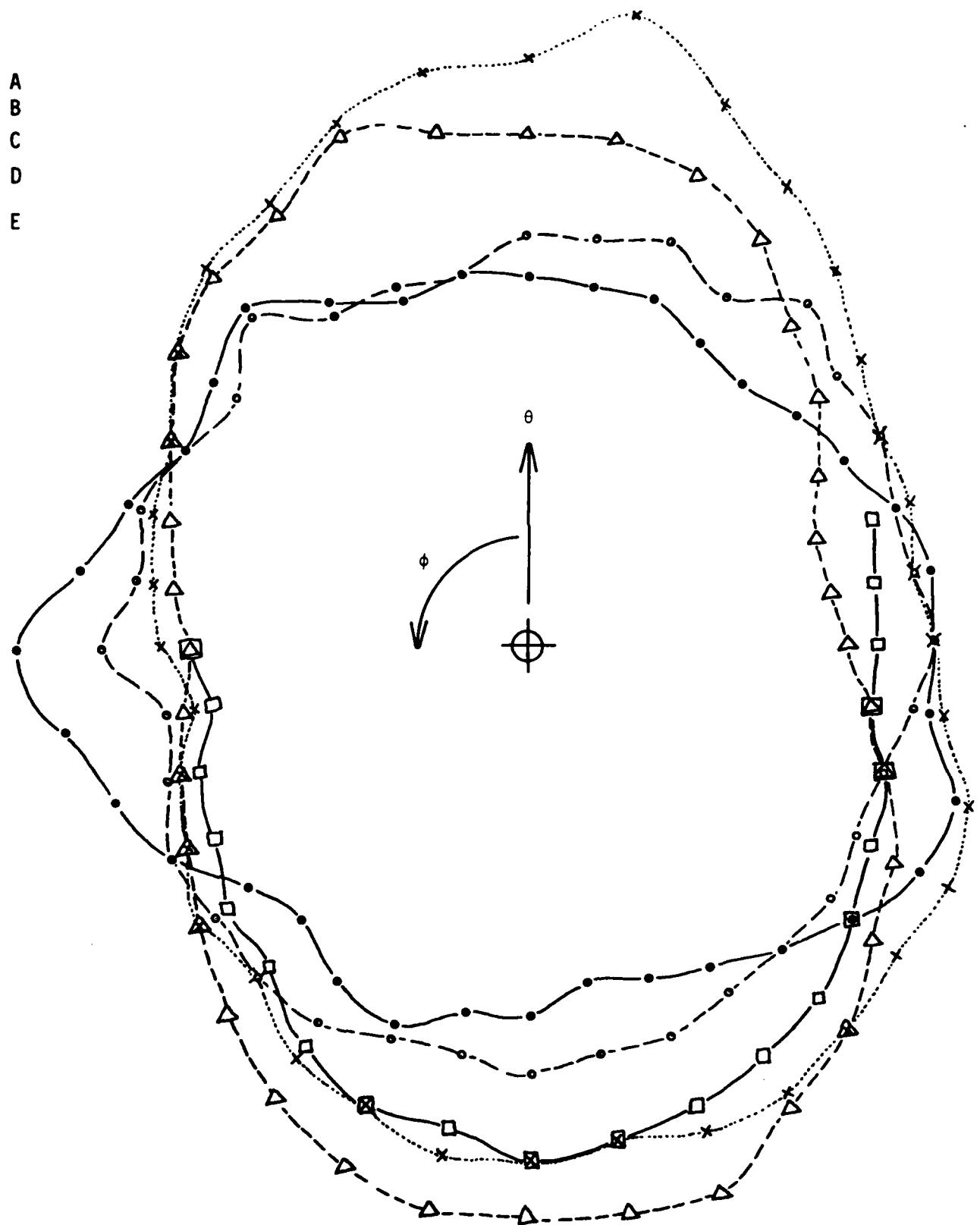
Fig. 12. This figure illustrates critical angle measurements on five
specimens of a titanium alloy with varying O_2 content. The O_2
content increases from A to E. Curves for A and B seem to be
more or less isotropic (circular pattern) while C,D,E fall in
a distinctly elliptical pattern suggesting that a major crystal-
line anisotropy enters for specimens C,D,E. This change in
crystal structure appears to occur at a certain threshold O_2
content characteristic of specimen C.

5.0 IMAGING EXPERIMENTS

Perhaps the most interesting application of the Rayleigh critical angle phenomenon is in imaging near surface mechanical properties. As mentioned earlier, we are not yet armed with computer algorithms that would allow a complete working out of local elastic constants from measurements. However, one can indirectly detect changes in these elastic properties by noting changes in the reflected amplitude $R(\theta)$ and the phase $\psi(\theta)$ at the point detector (see Fig. 1). The local changes over the interface constitute an "image" of whatever (flaw, discontinuity, etc.) it is that is responsible for a change in the elastic properties of the solid near this surface. As an example of what can be done, consider the images produced in Figs. 13 through 16. In each case, except for Fig. 16, the specimen was aluminum, which as we have seen is very nearly isotropic even in the crystalline state (see Fig. 11).

Because the reflected longitudinal wave is modulated by the interface wave and because the interface wave extends roughly one shear wavelength ($\lambda_T = C_T/f$) into the solid, these images provide information on the solid within λ_T of the liquid-solid boundary.

The images in Figs. 13 through 16 were made by scanning the sample (using a computer controlled x-y scanner not shown in Fig. 2). Targets scanned ranged from flat-bottomed holes in aluminum to a piece of fine grained granite. Note, as in Fig. 13, that whenever the boundary conditions are insufficient to generate a surface wave ($\theta \neq \theta_R \geq \theta_T$) or the depth of the discontinuity is greater than the surface wave penetration (λ_T) as in Fig. 14, no discontinuity can be seen in the images.

Figure 15 illustrates the result of imaging a "stress-dislocation" field resulting from a steel ball bearing being pressed into an aluminum sheet [28] – [30]. Figure 16 illustrates images of a granite specimen showing what appears to be individual crystal grains.

PHASE IMAGES $\psi(\theta)$ AMPLITUDE IMAGES $R(\theta)$

θ_c θ_c

$\theta_c + .70°$ $\theta_c + .70°$
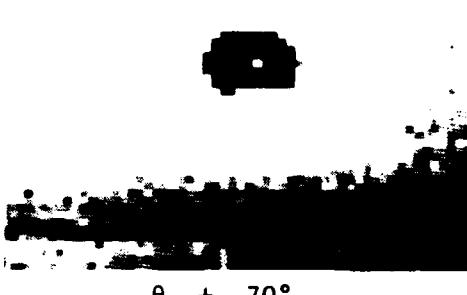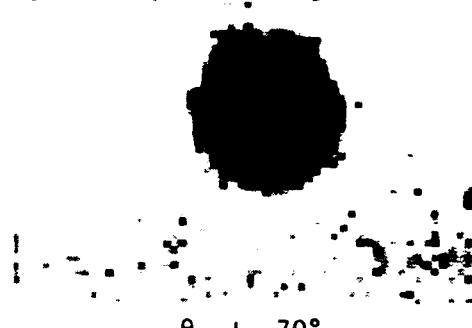
$\theta_c + 1.4°$ $\theta_c + 1.4°$

Fig. 13.   Phase $\psi(\theta)$ and amplitude $R(\theta)$ images of a .6 cm diameter flat-
          bottomed drill hole .8 mm from the surface of an aluminum plate
          .9 cm. thick.   Images at the top of the figure were made at the
          critical angle for aluminum ($\simeq 31°$) while those below were made at
          successively larger angles.   Note that as θ increases, the conditions
          for surface wave generation are eventually ruined and the images grow
          steadily worse.   The frequency for these experiments was 3.75 MHz.
          A lens and point receiver similar to that shown in Fig. 1 was
          employed.   The hole images are somewhat eliptical in shape owing to
          the incorrect aspect ratio of the monitor.

PHASE IMAGES $\psi(\theta)$ AMPLITUDE IMAGES R (θ)

7.0 MHz   7.0 MHz

3.6 MHz   3.6 MHz

1.86 MHz   1.86 MHz

Fig. 14. Phase $\psi(\theta)$ and amplitude R(θ) images of a series of .6 cm diameter
          flat-bottomed drill holes at varying depths (.4, .8 and 1.6 mm)
          from the surface of an aluminum plate .9 cm thick. All images were
          made at the critical angle for aluminum ($\simeq$31°) and varying the
          frequency as shown. Note that as the frequency (f) increases, the
          depth of penetration of the surface waves ($\lambda_T \simeq C_T/f$) decreases,
          and for a frequency of 10 MHz (not shown) the hole at .4 mm depth is
          no longer visible for example.

PHASE IMAGE ψ(θ)   AMPLITUDE IMAGE R(θ)

STRESSED REGION

PHASE IMAGE   AMPLITUDE IMAGE

EDGE OF PLATE

Top View

3 mm

Cross Section

3 mm   0.8 mm
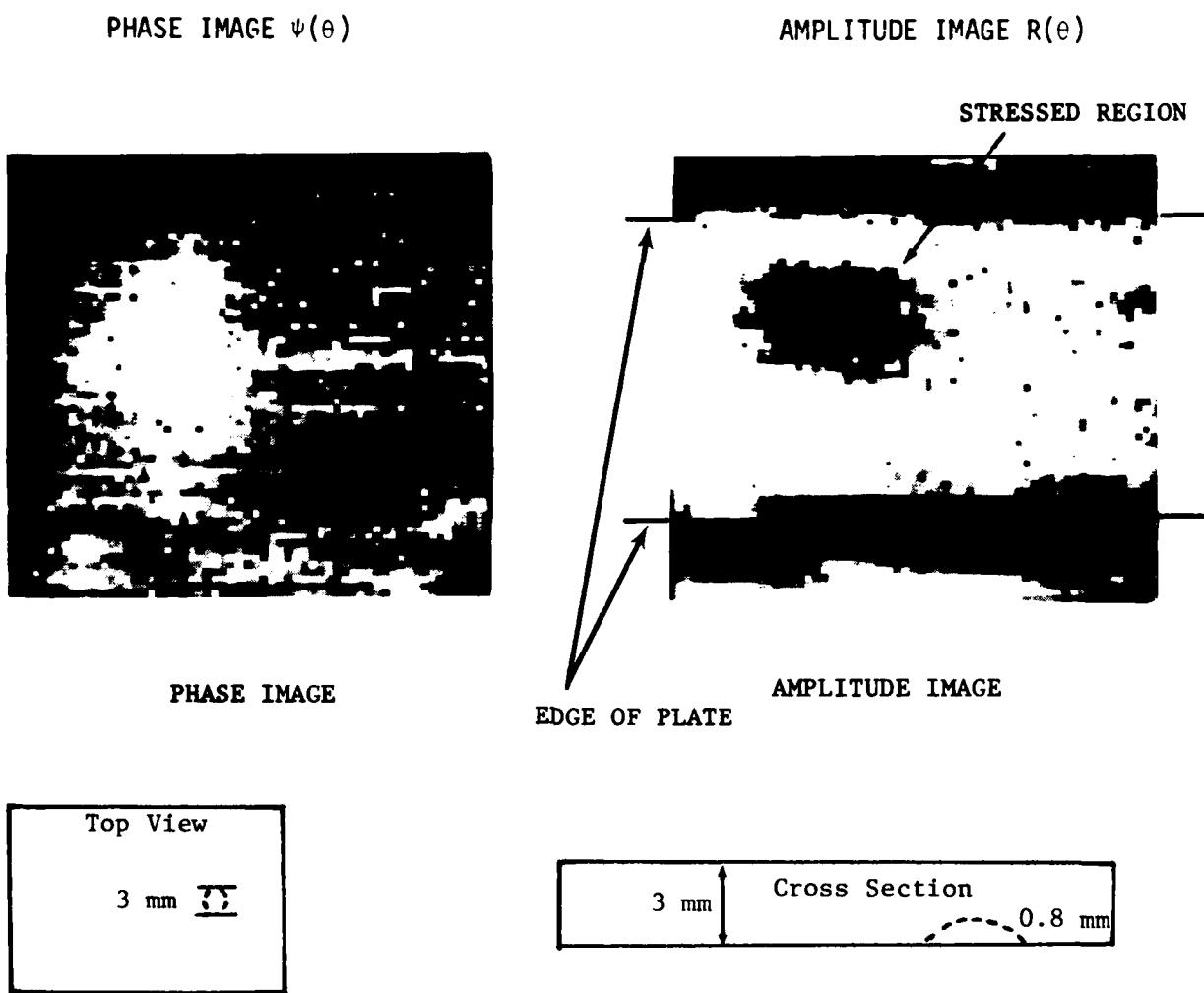
Fig. 15. Phase ψ(θ) and amplitude R(θ) images of a stress-dislocation
          field in a 3.2 mm thick aluminum plate in which a 4.8 mm steel
          ball bearing was pressed to a depth of .8 mm. The frequency
          chosen was 3.75 MHz but the critical angle (not recorded) was
          that of the flaw itself and not the aluminum (≈31°).

PHASE IMAGE $\psi(\theta)$ AMPLITUDE IMAGE $R(\theta)$
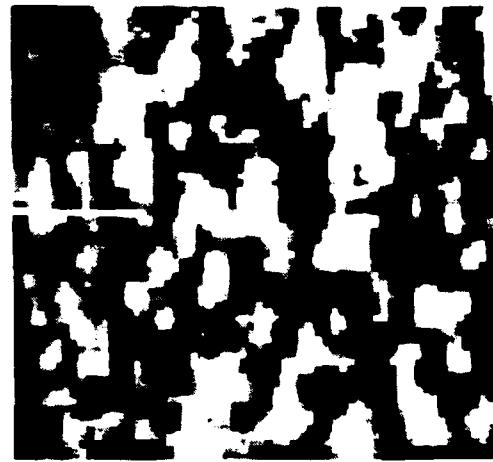

Fig. 16. Phase $\psi(\theta)$ and amplitude $R(\theta)$ images of a fine grained granite
          specimen (1-2 mm diameter grains) at a chosen incident angle of
          29.5°. The frequency was 3.75 MHz. Both phase and amplitude
          images show what appear to be individual crystal grains (3.8 cm
          scan length).

The qualitative interpretation of these images is clear but the
quantitative interpretation has yet to be carried out since it involves
very complex changes in the boundary conditions over short distances
near the discontinuities. In principle, such calculations can be
made for the amplitude images, however there are questions regarding
the phase images and the information on which they are based.

Figures 17 and 18 illustrate an interesting situation that is
sometimes encountered. Phase shifts are typically 360° on passing
through the critical angle. That is, the phase normally goes through
a change where it continually increases (or decreases) but returns to
0° (360°). Sometimes, however, a curve of the type shown in Fig. 17
occurs. The phase advances, retards, and then advances again returning
to zero. This effect can be seen on the same sample and does not seem
to be related to electronic noise or other similar problems. We also
know that these phase measurements are unaffected (directly) by higher
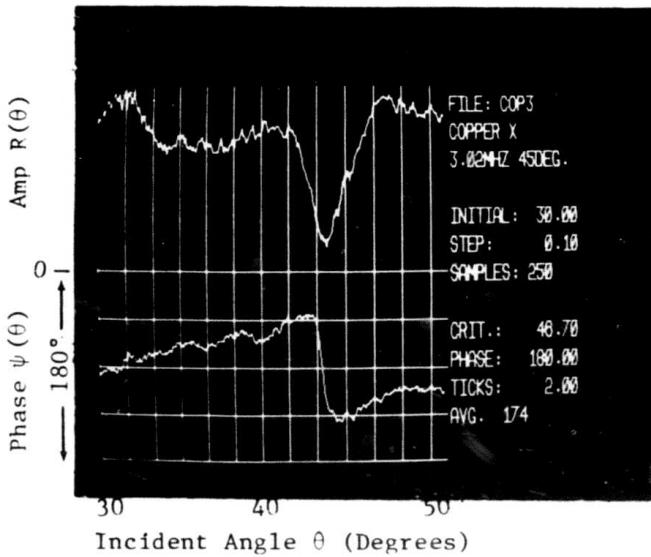
File name
Specimen name
Frequency or other comments

Initial angle θ
1° increments (θ)
Number of angular positions

Critical angle (R(θ) minimum)
Phase range on ψ(θ) graph
Spacing on ψ(θ) graph
Number of measurements averaged
at each angular position

Fig. 17. Reflected Amplitude R(θ) and Phase ψ(θ) for a Cu Single Crystal (100 Plane) at 20°C and a Frequency of 3.0 MHz. These curves (ψ(θ)) illustrate the phase "reversal" effect. Compare with a "normal" type phase curve ψ(θ) such as that illustrated in Fig. 18.
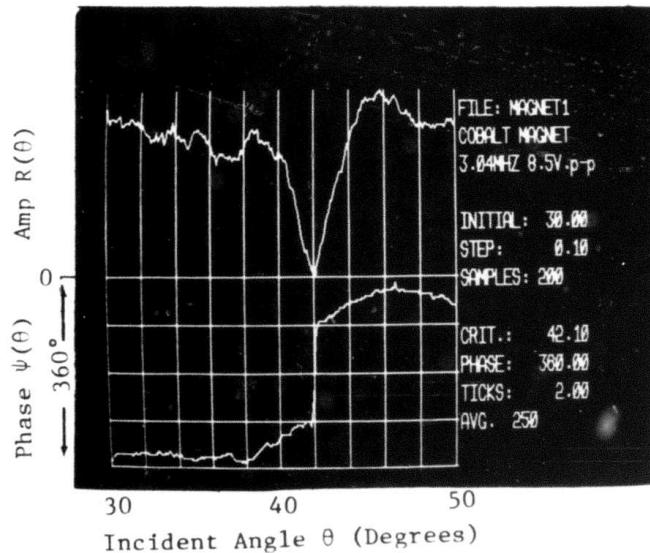
Fig. 18. Reflected Amplitude R(θ) and Phase ψ(θ) for a Cobalt Powder Composite Showing a "Normal" Phase Curve ψ(θ) at 20°C at a Frequency of 3 MHz. Note that the phase shift for these "normal" phase curves is typically 360°, whereas the curves showing the "reversal" (Fig. 17) is less. The critical angle for this specimen is located at 42°. The choice of the particular materials illustrated in Figs. 17 and 18 is arbitrary. Many different materials illustrate these effects. The same specimen often exhibits both types of curves.

-31-

harmonics since our phase meter sees only the fundamental. However, we cannot rule out the possibility that a signal at the fundamental frequency produced by nonlinear effects (intermodulation of harmonics, for example) is distorting the "normal" phase curve near the critical angle.

Regardless of the ultimate explanation for such effects, it is clear that phase information and especially phase images are not to be trusted unless and until these problems are cleared up. This is not the case with the amplitude images which would be little altered by contamination with a small signal at the fundamental frequency.

6.0 NONLINEAR EFFECTS

We have delayed a detailed discussion of nonlinear effects until
the last, for two reasons. First, as emphasized in the beginning of
this report, many features of the critical angle phenomenon (such as
the magnitude of various critical angles) are well accounted for, at
least in principle, by linear theory supplemented by anisotropy.
Second, the effects, that we have observed which can be attributed to
nonlinearities, are not yet sufficiently well understood to place them
in a position of prominence.

It is known that both water and a typical solid are nonlinear,
and that water is more nonlinear (has a shorter discontinuity length,
for example) than the typical solid [17], [18], [37]. Thus, we
expect to see nonlinear effects due to the water, and possibly the
solid as well, at the critical angle where the amplitude in the
solid increases dramatically.

6.1   Spectral Measurements

A dynamical physical system, such as the water path-solid combina-
tion in our experiments, can be characterized by its frequency response.
That is, the frequency spectra of the signals propagating through the
system may be analyzed to determine the response of the system to various
inputs. Any anomalies, such as nonlinearities, will then be characterized
by changes in such spectra as a function of certain variables (source
voltage, angle of incidence, etc.). Although it is very difficult to
obtain absolute spectral information in a complex electronic and physical
system, owing to many coupled transfer coefficients, it is possible to
obtain relative spectral information as certain quantities, such as
incident angle θ, are varied. We have made such relative spectral
measurements on nonspecularly reflected longitudinal waves (reflected
and radiated by leaky surface waves) at and near various critical angles.

This information provides insights into the nature of the scattering process as a function of the angle of incidence (θ) of the longitudinal waves and other relevant variables.

A typical spectral analysis of the reflected wave is performed by first finding a suitable frequency at which a sharp minimum of $R(\theta)$ occurs. A suppression filter is then adjusted to cut out this frequency while passing the higher harmonics. It is necessary to suppress the fundamental owing to the fact that our digitizer has only 8-bit accuracy, and the higher harmonics are small relative to the unfiltered fundamental. Signals are digitized at a 20 MHz rate and then Fourier analyzed to obtain the resultant frequency spectrum. An example of such a spectrum is illustrated in Fig. 19.

Samples of mica, optical glass and aluminum (single crystal) were examined at the same fundamental frequency (4.5 MHz) at several different source voltage settings using a 4.5 MHz suppression filter.

6.1.1 <u>Mica Standard</u>. The question of whether nonlinear effects due to the water (and possibly the solid) are important in interpreting critical angle data is a complex one, owing to the fact that the reflection coefficient is capable of drastically altering the harmonic content generated solely in water (not to mention the solid).

Consider the observations made on a thin (.002 in.) reflecting mica window. Figure 20(a) through(c) illustrates data obtained on the fundamental (4.5 MHz) and the second harmonic (9.0 MHz) for angles of incidence ranging from 15 to 45°. Before the data was digitized, it was first passed through a 4.5 MHz (-30 DB) suppression filter (which has very little effect on the higher harmonics) amplified and then ligitized at a 20 MHz rate (8 bit accuracy). The data was then Fourier analyzed using an FFT routine (on the IBM personal computer) and the amplitudes were then plotted as shown in these figures. Data at three different source voltage levels (10, 8, 6 volts) is illustrated in these figures.
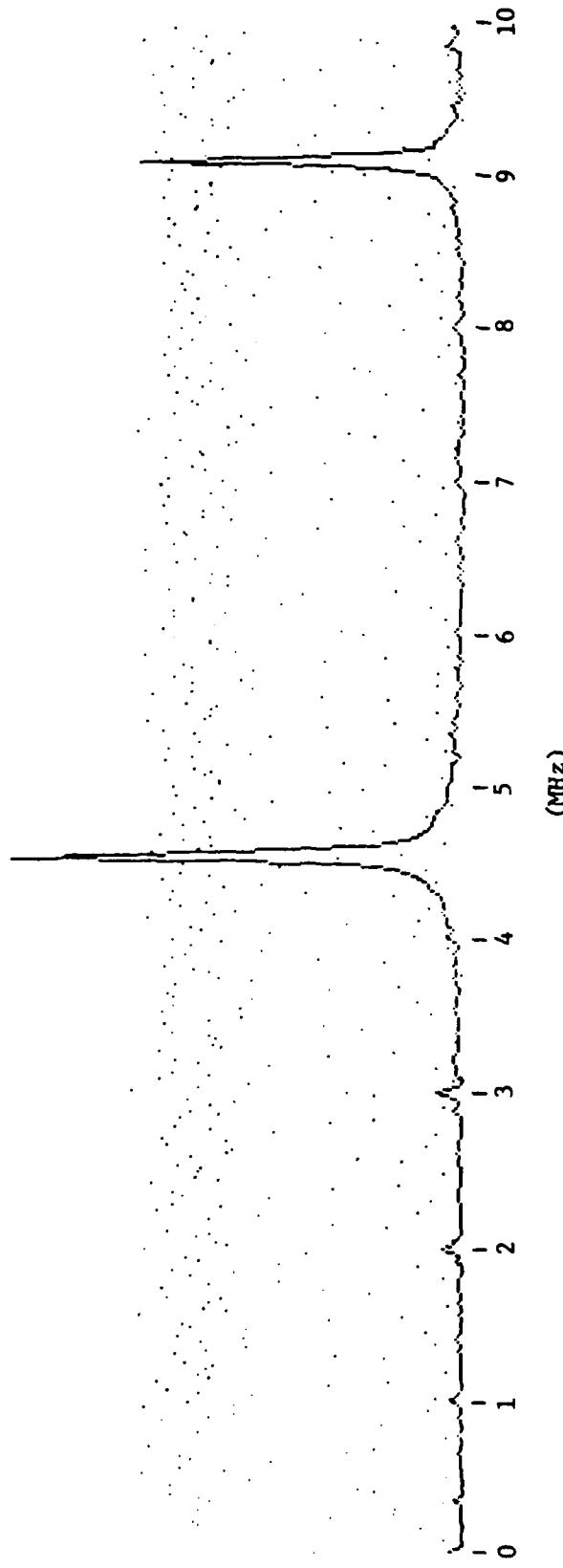
Fig. 19. Typical spectrum. In this case the source voltage was 8 volts and the point detector was located on the axis of a 4.0 inch focal length lens (4.5" from the lens). The fundamental frequency (4.5 MHz) was suppressed by a -30 DB filter that passed the second harmonic (9 MHz) unaltered.

RELATIVE AMPLITUDES

MICA

1st

2nd

θ (Degrees)

20.00   25.00   30.00   35.00   40.00

Fig. 20 (a)   Source voltage 10V

RELATIVE AMPLITUDES

MICA

1st

2nd

θ (Degrees)

20.00   25.00   30.00   35.00   40.00
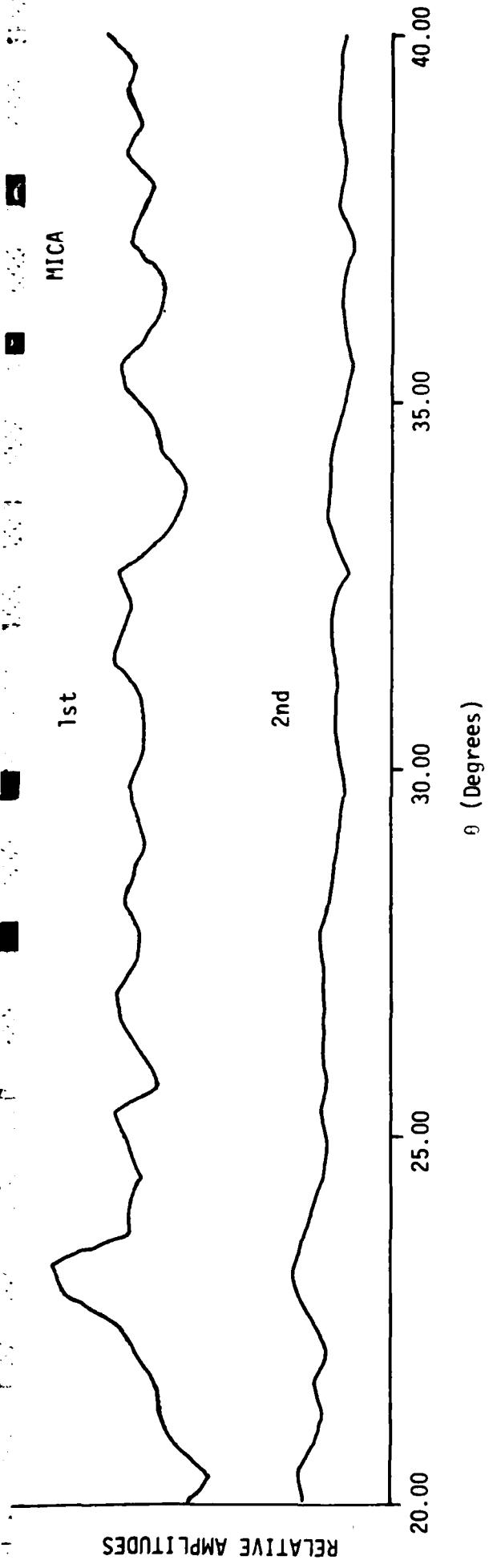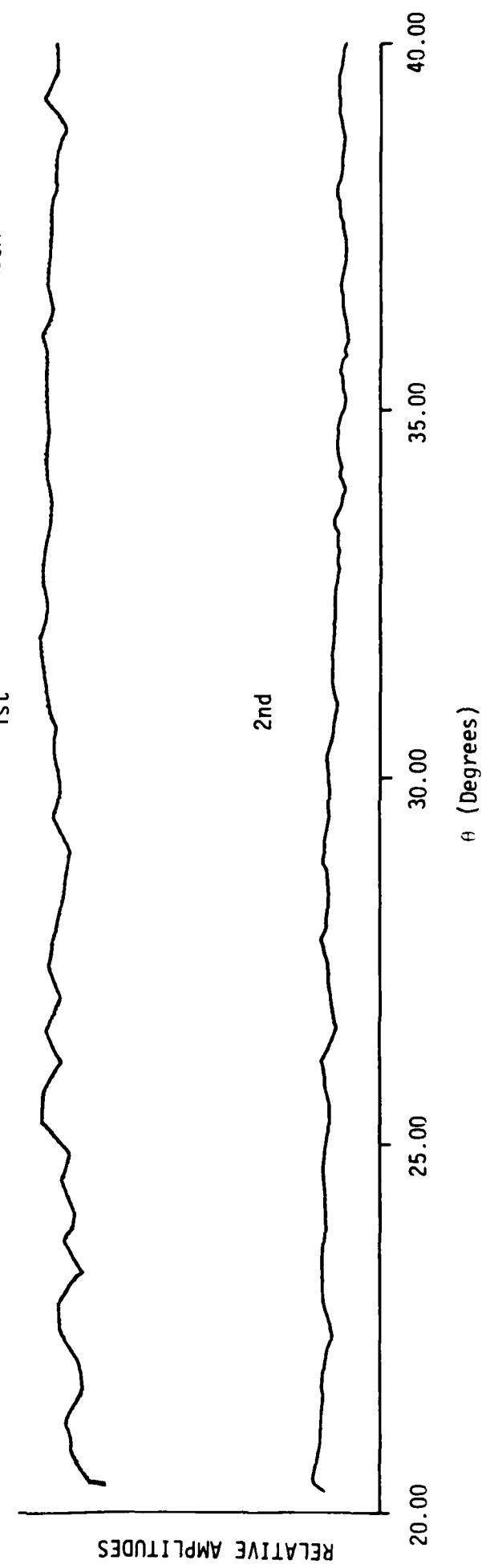
Fig. 20 (b)   Source voltage 8V

-36-
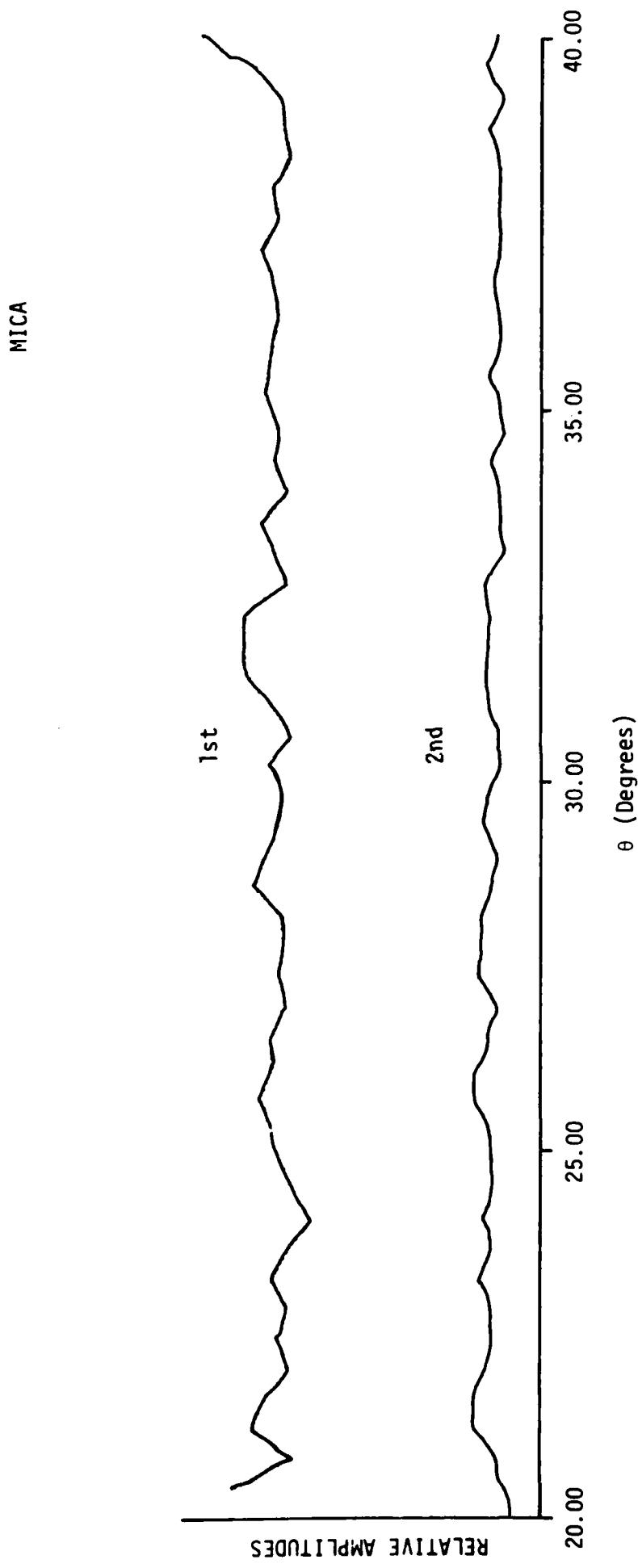
Fig. 20 (c) Source voltage 6V

Fig. 20.   Reflected amplitudes as a function of θ for a thin (.002 in.) mica window (air backed). Fundamental frequency is 4.5 MHz. Source voltages varied from 10V to 6V. The fundamental was suppressed by a -30 DB filter before digitizing and Fourier analyzing the received signal. Relative amplitudes of the fundamental and second harmonic obtained from the Fourier analysis are illustrated. Note that the samll variations of amplitude are not reproducible. These are due primarily to density fluctuations in the water path which scatter or deflect the incident beam. If we average several such curves, these variations tend to disappear.

-37-

The first thing to be noted about the data is that the signals for each voltage setting contain a second harmonic component. Second, the amplitude of both the fundamental and the second harmonic (at each voltage setting) is essentially constant at its average value for any angle of incidence θ. Third, the ratio of the second harmonic amplitude to the fundamental amplitude is essentially independent of the voltage setting. This last observation does not imply that both amplitudes are independent of the voltage setting. In fact, the average amplitude of the fundamental should be taken to be roughly proportional to the source voltage setting.

These observed facts lead to several important conclusions regarding the nature of the source, the effects of the mica reflector, and the nature of the nonlinear effects in the water path. The fact that (A_2/A_1) is essentially independent of the voltage settings is very significant. It means that the effect of the mica reflector completely cancels any second harmonic generated in the water and passes only the initial second harmonic contamination at the source.

To see this, we first note that an increase in the voltage setting (call it k) causes the fundamental amplitude A_1 to increase in the same proportion as the second harmonic amplitude A_2, thereby maintaining the ratio $kA_2/kA_1 = A_2/A_1 = $ constant. Thus, the second harmonic we see on the mica reflector is only that due to contamination at the source. This is not to say that there are no higher harmonics produced by the source. In fact, these are present, but as Breazeale has emphasized, if each frequency component is shifted by 180° (for any reason) when the waves return to the receiver (source reflector distance = reflector - receiver distance), they will have no higher harmonics present other than initial contamination. Now we also know that the mica phase shifts all incident waves by 180° so that any observed component at the receiver is merely the contamination present at the source. This explains in a simple way why A_1/A_2 is constant with source voltage. The source voltage (10, 8, 6 volts) definitely produce higher harmonics due to nonlinearities, but all of these are always eliminated by propagation.

6.1.2 <u>Measurements Along the Lens Axis</u>. That a second harmonic component due to nonlinear effects is actually present along the water path is demonstrated by the following experiments. The results illustrated in Figs. 21 through 23 were obtained by examining the signals along the axis of the acoustic lens including the focal region, which in this case is located at 4.0 inches from the lens (geometric focus).

Because the beam is converging, the amplitudes of both the fundamental and any second harmonic contamination that originate at the source will generally increase as the focus is approached, and likewise would be expected to diminish beyond the focus. Note that the fundamental component has just such a behavior, i.e., it is essentially symmetric about its maximum amplitude. It should be noted, however, that the maximum amplitude occurs at a position some-what closer to the lens than the geometric focus.

The second harmonic (Figs. 22 has a considerably different behavior than the fundamental. Note that it is not symmetric about its maximum value. This can only mean that a nonlinear process is creating excess second harmonic components over and above the input contamination. In all of these figures, it is clear that the amplitudes A_2, A_1 generally increase with source voltage in a way that demonstrates nonlinear behavior in the water. For example, if the water were purely linear, a source voltage factor, k, would result in a constant ratio $kA_2/kA_1 = A_2/A_1$ = constant. This is clearly not the case. As the source voltage is increased, this ratio increases at the detector for essentially all distances from the source indicating the nonlinear production of a second harmonic.

6.1.3 <u>Optical Glass</u>. The position of the critical angle can depend on the frequency and this fact can also affect the behavior of the second harmonic amplitude relative to the amplitude of the fundamental. To see this, consider the data taken on optical glass as shown in Fig. 24(a) through (e). Frequency (fundamental) and amplitude (in some

Fundamental 4.5 MHz

Relative Amplitude

Distance from Lens (Inches)
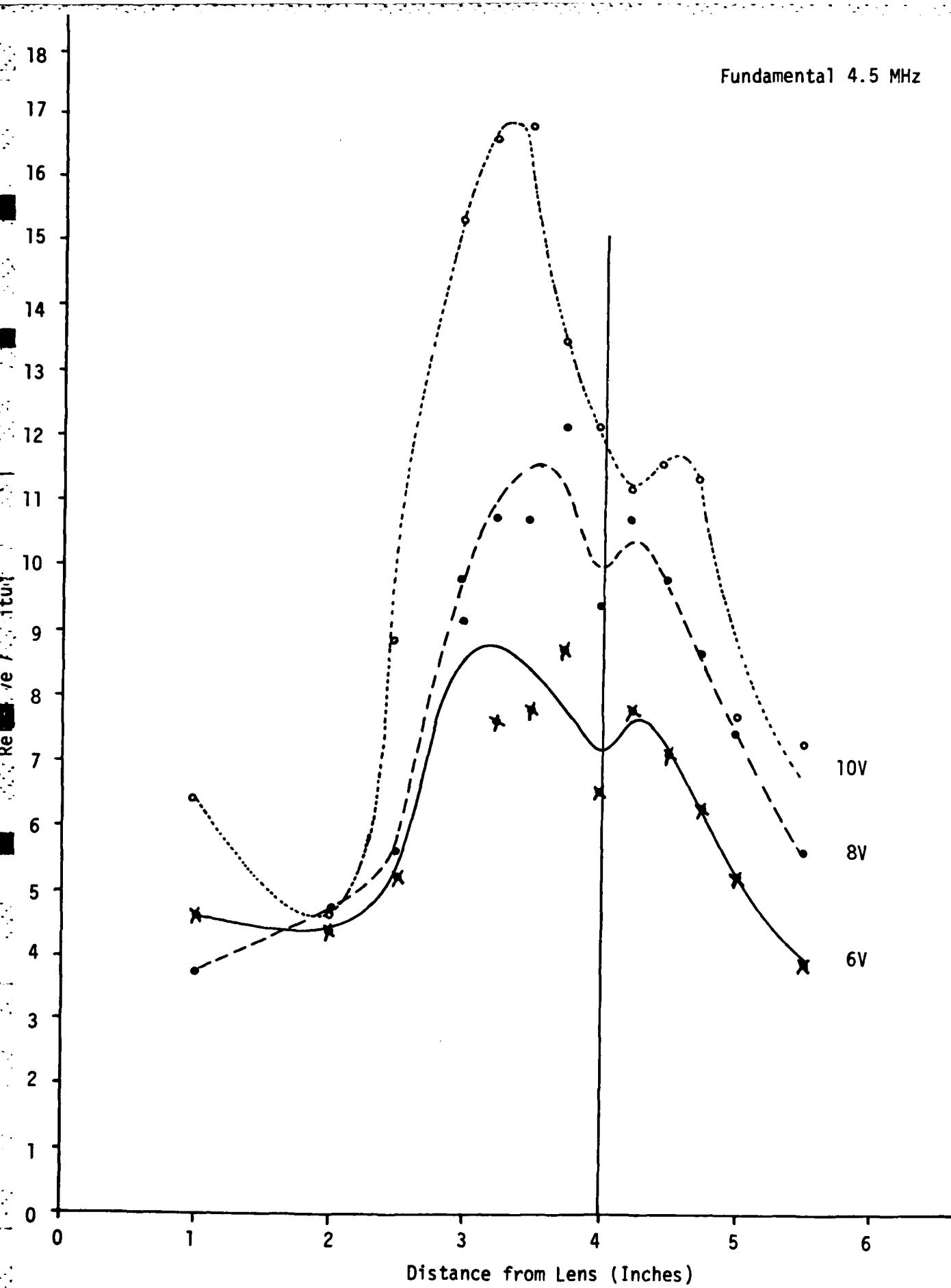
Fig. 21. Amplitudes of the fundamental (4.5 MHz) at various distances from the 4.0 in. focal length lens. Source voltages were 10, 8, and 6 volts.
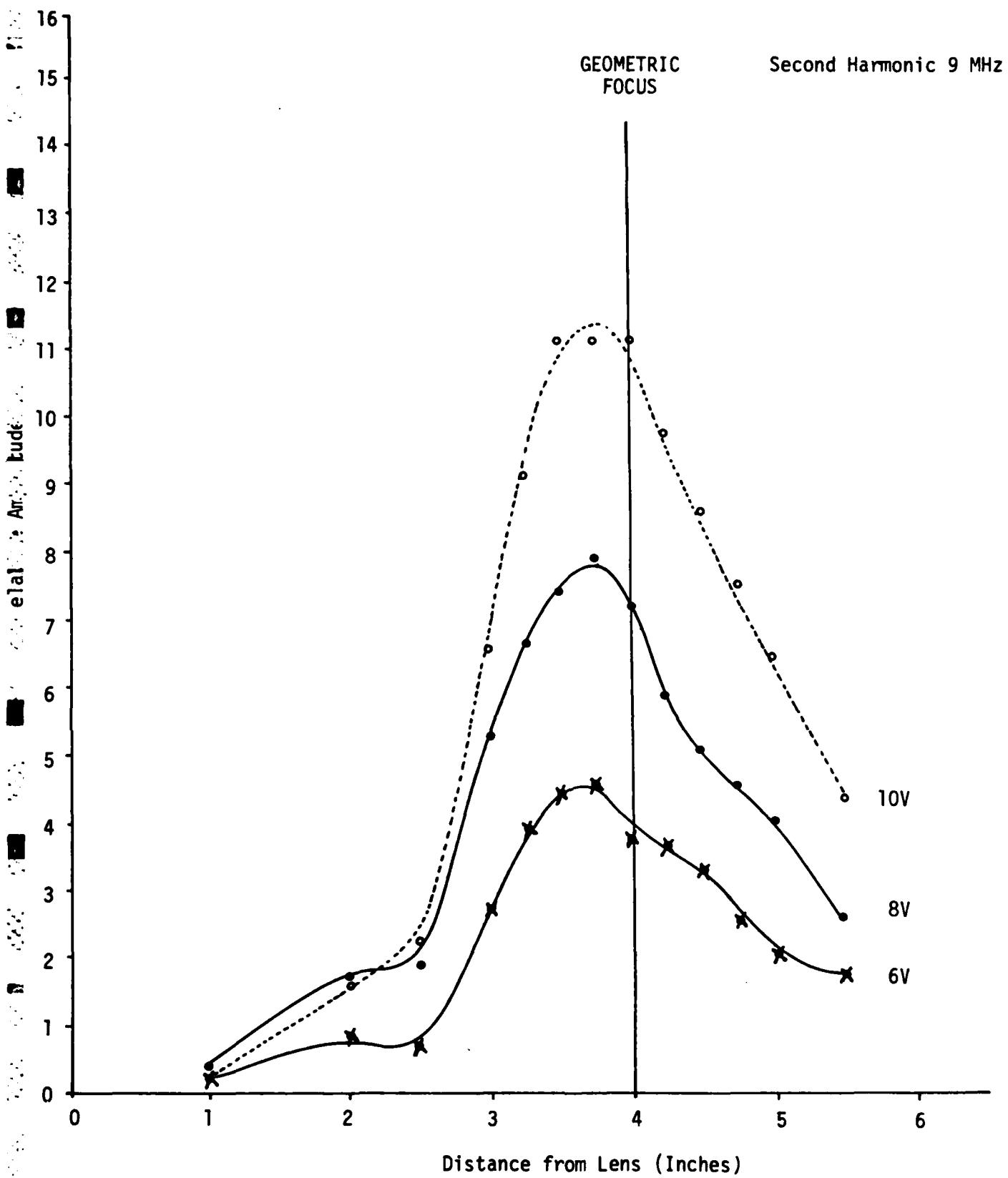
Fig. 22. Amplitudes of the second harmonic (9 MHz) at various distance from the 4.0 in. focal length lens. Source voltages were 10, 8, and 6 volts.
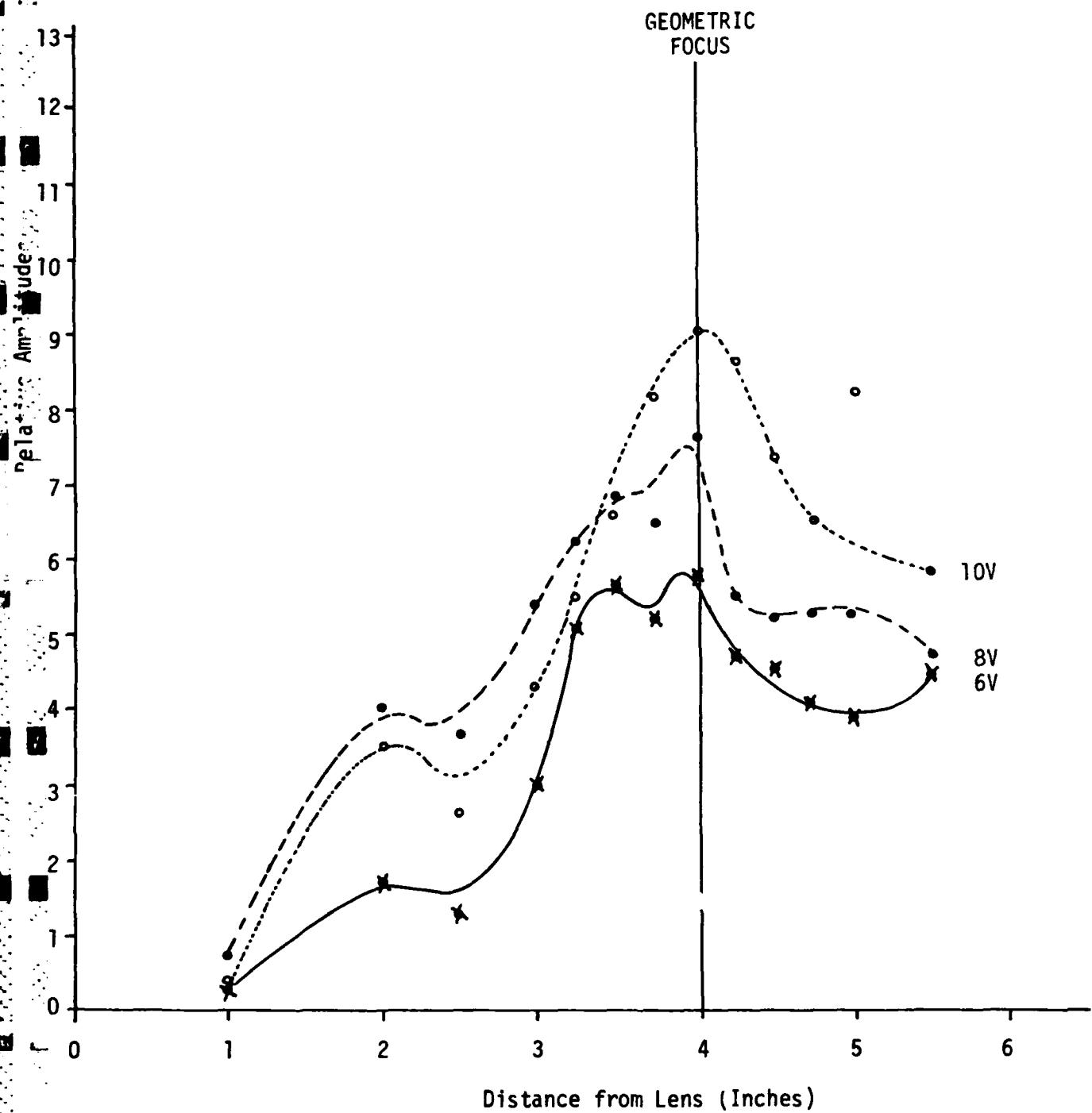
Fig. 23. Ratio of second harmonic amplitude (9 MHz) to amplitude of the fundamental (4.5 MHz) at various distances from the 4.0 in. focal length lens. Source voltages were 10, 8, and 6 volts.
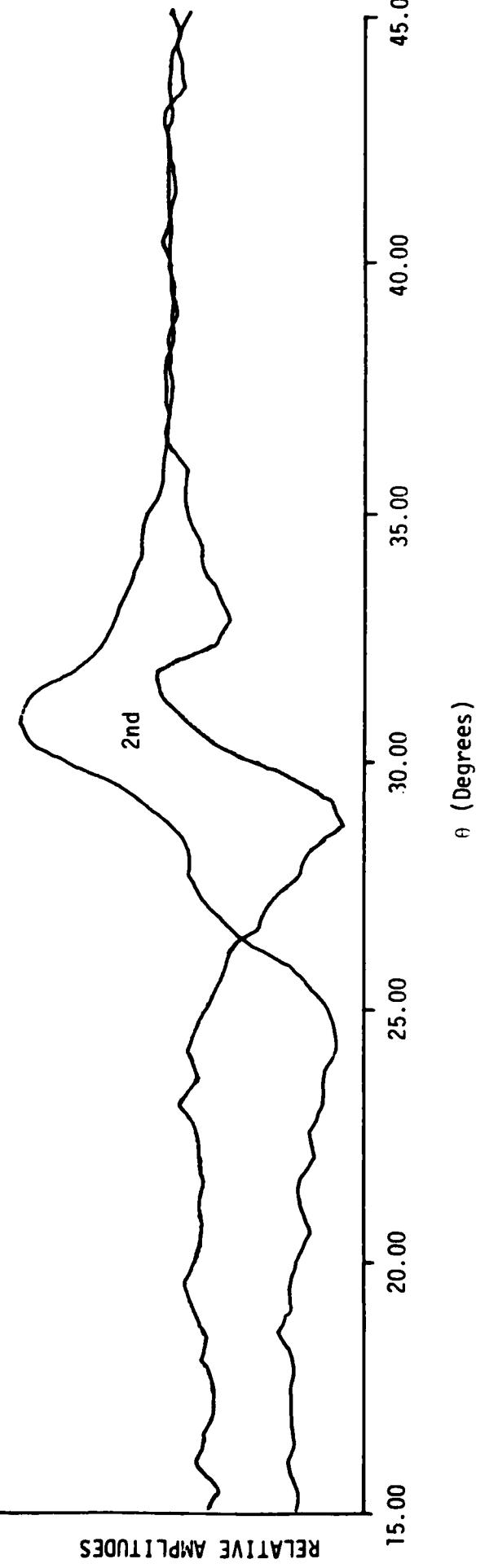
Fig. 24 (a) Source voltage 10V
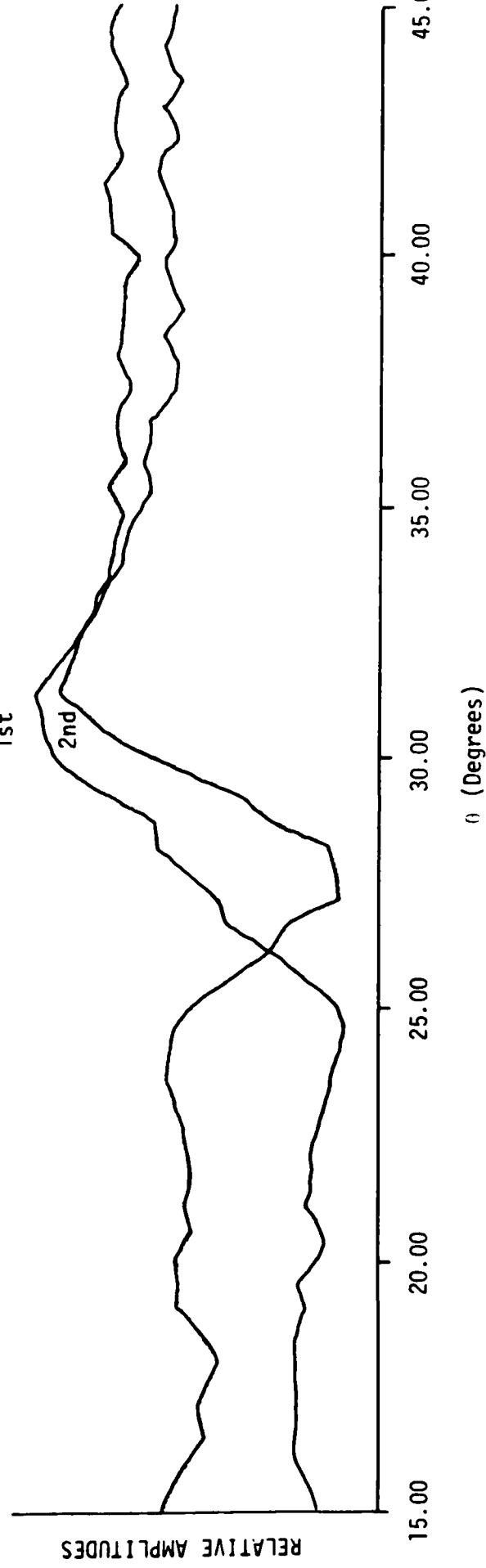
Fig. 24 (b) Source voltage 9V

OPTICAL GLASS

RELATIVE AMPLITUDES

θ (Degrees)

1st

2nd
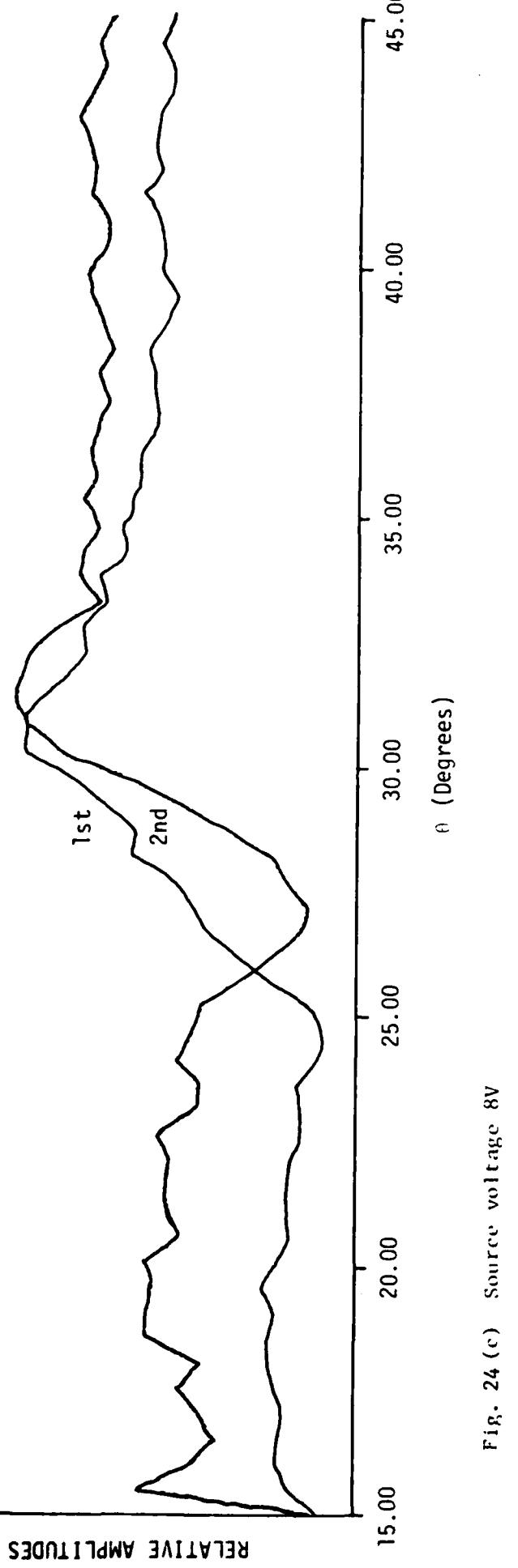
Fig. 24 (c) Source voltage 8V

RELATIVE AMPLITUDES

θ (Degrees)

1st

2nd
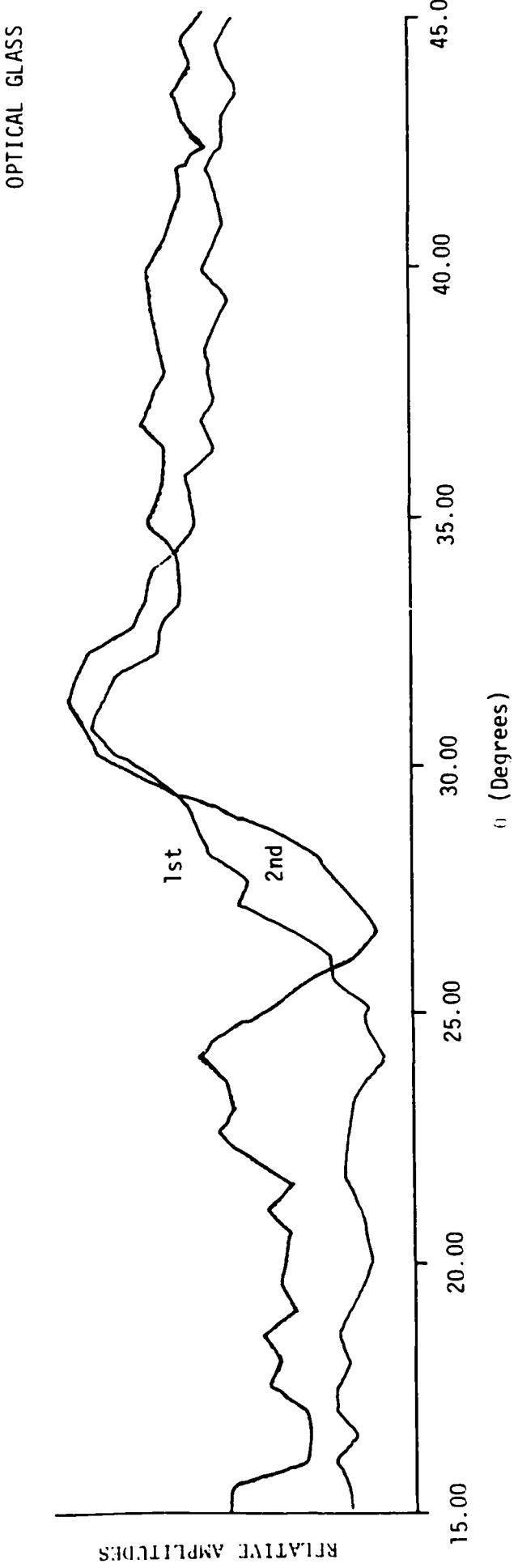
Fig. 24 (d) Source voltage 7V

-44-

OPTICAL GLASS

RELATIVE AMPLITUDES

1st

2nd

15.00   20.00   25.00   30.00   35.00   40.00   45.00

θ (Degrees)
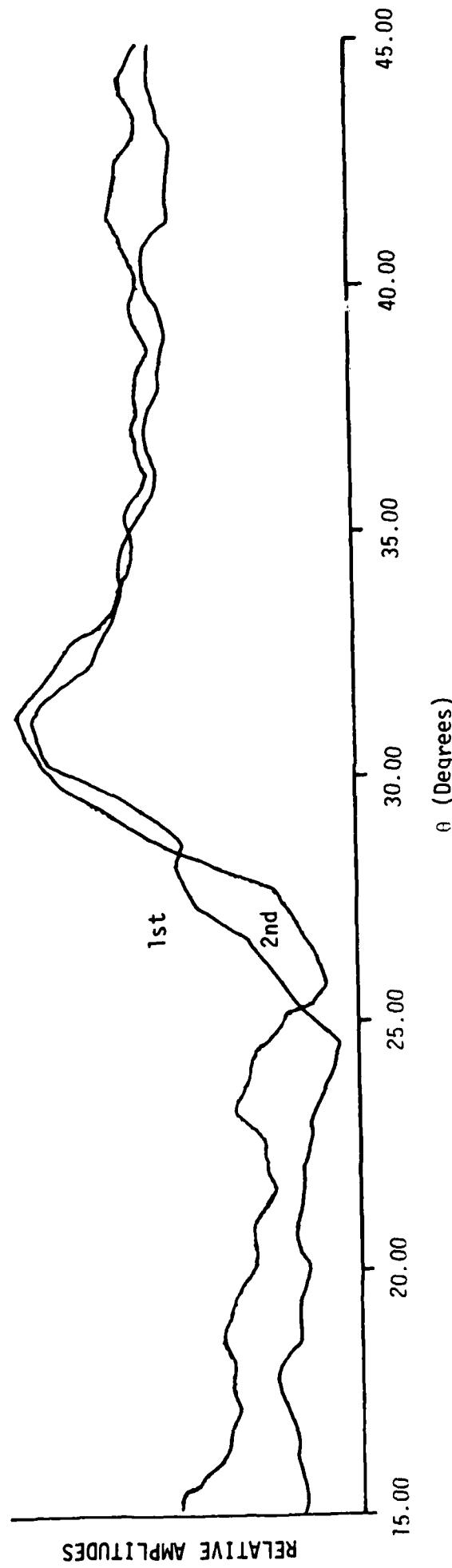
Fig. 24 (e) Source voltage 6V

Fig. 24. Relative reflected amplitudes of the fundamental and second harmonic (9 MHz) on optical glass (-30 DB filter used to suppress fundamental) for different source voltages and angles of incidence θ. See note on amplitude variations in Fig. 36.

-45-
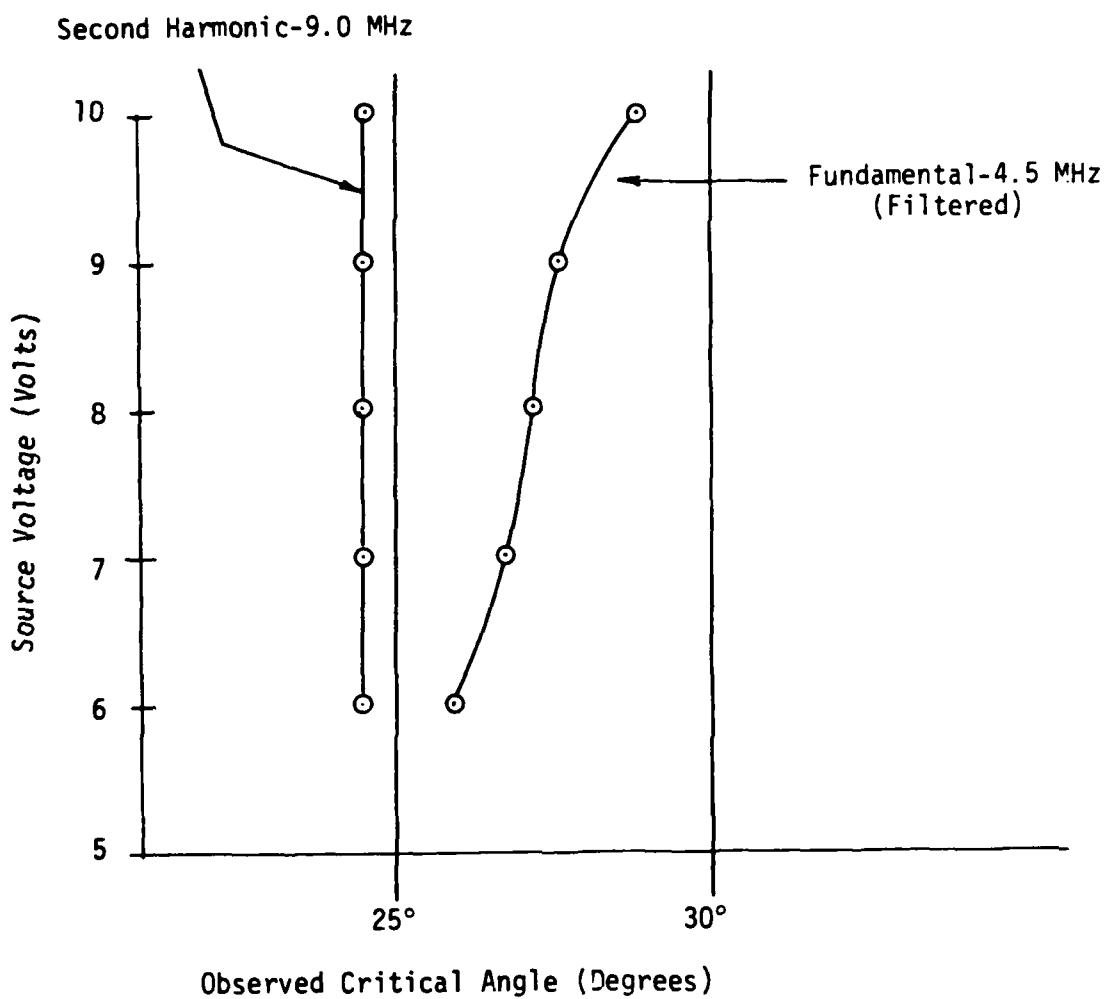
OPTICAL GLASS

Fig. 25. Position of critical angles for second harmonic and fundamental on optical glass as a function of source voltage.

cases) were chosen to be the same as for the data taken on the mica window.

Data was taken for source voltage settings of 10, 9, 8, 7, and 6 volts. The data at each voltage setting is characterized by a second harmonic amplitude which goes to a minimum at an angle ranging up to 4° less than the critical angle characterizing the position of the minimum of the fundamental amplitude. Moreover, the postion of the second harmonic minimum amplitude is constant as a function of the source voltage, whereas the position of the minimum of the fundamental amplitude steadily shifts to lower values as the source voltage is reduced (see Fig. 25).

6.1.4 <u>Discussion</u>. It has been stressed by Breazeale and others that if each component in an incident sawtooth waveform is shifted by 180° and allowed to propagate without attenuation, it will eventually "heal" and be converted back to the fundamental at the detector, provided the detector is at the same distance from the reflector as the source is from the reflector.

Now even if we ignore frictional attenuation (geometric attenuation is the same for each frequency and can safely be ignored) which differs for each frequency component, we certainly cannot ignore the amplitude modulation of each component near critical angles which vary. If the critical angle is the same for each harmonic and the shape of the amplitude minima is identified, then the amplitude modulation that occurs when the critical angle is approached should have little effect on the "healing" process described above.

In conclusion, it is not possible at this time to say that we have seen effects due to nonlinearities in the solid, but there is no doubt that nonlinear effects in the water coupled with the particular properties of the solid can significantly effect the resultant harmonic content in the received signal. This is clearly an area needing further study.

7.0 CONCLUSIONS

We have performed numerous critical angle experiments on a
variety of samples ranging from single crystals to polycrystalline
alloys and glasses. Two basic conclusions can be drawn from this
work: 1) simple linear equations of motion (which include aniso-
tropy) suffice for an approximate description of the observations
(for example, the value of various critical angles can be calculated
from a knowledge of second order elastic constants alone); 2) certain
observations at and near the critical angle, involving the production
of anomalous harmonics, imply that the nonlinear characteristics of
the water (and possibly the solid) cannot be ignored and need further
study. Moreover, the body of knowledge gained so far shows that our
new measuring apparatus, using an acoustic lens, has the following
desirable features: a) it allows local measurements of the solid
properties to be observed and b) except for problems associated with
phase measurements of the reflected waves, experimental results are
essentially consistent with the work of others who used a different
experimental approach. We conclude that our goal of using a device
in practical flaw imaging work is reasonable and holds promise of
being a quantitative flaw imaging technique.

8.0 ACKNOWLEDGMENTS

9.0 REFERENCES

[1] A. Schoch, *Acustica 2*, 18 (1952).

[2] Brekhovskikh (1960).

[3] F. R. Rollins, Jr., "Ultrasonic Reflectivity at a Liquid-Solid Interface Near the Angle of Incidence for Total Reflection," *Appl. Phys. Lett.*, Vol. 7, No. 8 (1965).

[4] F. L. Becker and R. L. Richardson, "Influence of Material Properties on Rayleigh Critical Angle Reflectivity," *J. Acoust. Soc. Am.*, 51, 1609 (1972).

[5] F. L. Becker and R. L. Richardson, "Ultrasonic Critical Angle Reflectivity," *Research Techniques in Nondestructive Testing*, edited by R. S. Sharpe, Academic Press, London, 91-130 (1970).

[6] V. M. Merkulova, *Sov. Phys. Acoust.*, 15, 404 (1970).

[7] H. L. Bertoni and T. Tamir, "Unified Theory of Rayleigh Angle Phenomena for Acoustic Beams at Liquid-Solid Interfaces," *Appl. Phys.* 2, 157-172 (1973).

[8] L. E. Pitts, "A Unified Theoretical Description of Ultrasonic Beam Reflections from a Solid Plate in a Liquid," Ph.D. Thesis, Georgetown University, Washington, D.C. (1976).

[9] L. E. Pitts and T. J. Plona, "Theory of Nonspecular Reflection Effects for an Ultrasonic Beam Incident on a Solid Plate in a Liquid," *IEEE Transactions on Sonics and Ultrasonics*, Vol. SU-24, No. 2 (1977).

[10] T. D. K. Ngoc and W. G. Mayer, "Numerical Integration Method for Reflected Beam Profiles Near Rayleigh Critical Angle," *J. Acoust. Soc. Am.*, Vol. 67, 1149-1152 (1980).

[11] I. A. Viktorov, *Rayleigh and Lamb Waves, Physical Theory and Applications*, Plenum Press, New York (1967).

[12] B. P. Hildebrand and F. L. Becker, "Ultrasonic Holography at the Critical Angle," *J. Acoust. Soc. Am.*, 56, 459-462 (1974).

[13] G. L. Fitzpatrick et al., "Acoustical Imaging of Near Surface Properties at the Rayleigh Critical Angle," *Acoustical Imaging*, Vol. 12, edited by Eric A. Ash and C. R. Hill, Plenum Publishing Corp., New York (1982).

[14] L. M. Brekhovskikh, *Waves in Layered Media*, Academic Press, New York (1980).

[15] *Acoustical Imaging*, Vol. 12, edited by Eric A. Ash and C. R. Hill, Plenum Press, New York (1982).

[16] L. D. Landau and E. M. Lifshitz, _Theory of Elasticity_, Pergamon Press, New York (1975).

[17] R. T. Beyer, "Nonlinear Acoustics," _Physical Acoustics_, Vol. IIB, edited by W. P. Mason, Academic Press, New York (1965).

[18] Robert Beyer, "New Wave of Acoustics," _Phy. Today_ (1980).

[19] James A. Rooney and Wesley L. Nyborg, "Acoustic Radiation Pressure in a Traveling Plane Wave," _Am. J. Phys._, Vol. 40, 1825 (1972).

[20] J. D. Achenbach, _Wave Propagation in Elastic Solids_, North-Holland Publishing, New York (1973).

[21] B. A. Auld, _Acoustic Fields and Waves in Solids_, Vol. I & II, John Wiley, New York (1973).

[22] Rudolf Peierls, _Surprises in Theoretical Physics_, Princeton University Press, New Jersey (1979).

[23] R. E. Green, _Ultrasonic Investigation of Mechanical Properties_, Academic Press, New York (1973).

[24] F. E. Borgnis, "Specific Directions of Longitudinal Wave Propagation in Anisotropic Media," _Phys. Rev. 98_, 1000 (1955).

[25] K. Brugger, "Pure Modes for Elastic Waves in Crystals," _J. Appl. Phys. 36_, 759 (1963).

[26] Landolt-Bornstein, _Numerical Data and Functional Relationships in Science and Technology_, Vol. 2, edited by K. H. Hellwege and A. M. Hellwege, Springer-Verlag, New York (1969).

[27] G. W. Farnell, "Properties of Elastic Surface Waves," _Phys. Acoust._, Vol. VI, edited by W. P. Mason, Academic Press, New York (1970).

[28] Thomas J. Plona et al., "Ultrasonic Bounded Beam Reflection Effects a Liquid-Anisotropic-Solid Interface," _J. Acoust. Soc. Am. 56_, 1773 (1974).

[29] E. G. Henneke II, "Reflection-Refraction of a Stress Wave at a Plane Boundary Between Anisotropic Media," _J. Acoust. Soc. Am. 51_, 210-217 (1972).

[30] Edmund G. Henneke II and Gerald L. Jones, "Critical Angle for Reflection at a Liquid-Solid Interface in Single Crystals," _J. Acoust. Soc. Am._, Vol. 59, No. 1 (1976).

[31] O. I. Diachok and W. G. Mayer, "Crystal Surface Orientation by Ultrasonic Beam Displacement," _Acustica_, Vol. 26, 267-269 (1972).

[32] Orest I. Diachok et al., "Measurement of Ultrasonic Surface Wave Velocity and Absorptivity on Single-Crystal Copper," _Appl. Phys. Lett. 17_, 288 (1970).

[33] M. A. Breazeale, "Ultrasonic Studies of the Nonlinear Properties of Solids," <u>International Journal of Nondestructive Testing</u>, Vol. 4, Gorden and Breach, Great Britain (1972).

[34] K. A. Naugol'nykh, "Absorption of Finite-Amplitude Waves," <u>High Intensity Ultrasonic Fields</u>, edited by L. D. Rozenberg, Plenum Press, New York (1971).

[35] A. M. Sutin, "Influence of Nonlinear Effects on the Properties of Acoustic Focusing Systems," <u>Sov. Phys. Acoust. 24</u> (1978).

[36] A. L. Van Buren and M. A. Breazeale, "Reflection of Finite-Amplitude Ultrasonic Waves," I Phase Shift, <u>J. Acoust. Soc. Am.</u> <u>44</u>, 1014-1020 (1968) and II Propagation, <u>J. Acoust. Soc. Am. 44</u>, 1021-1027 (1968).

[37] M. A. Breazeale, Private Communication.